Received: 10 April 2019 | Revised: 25 July 2019 | Accepted: 26 July 2019 | Published on: 30 August 2019

DOI: 10.1002/qj.3627

RESEARCH ARTICLE

Quarterly Journal of the Royal Meteorological Society RMetS

Unravelling the March 1972 northwest Greenland windstorm with high-resolution numerical simulations

Mathias Tollinger[1] | Alexander Gohm[1] | Marius O. Jonassen[2,3]

[1]Department of Atmospheric and Cryospheric Sciences, University of Innsbruck, Austria

[2]Department of Arctic Geophysics, The University Centre in Svalbard, Norway

[3]Geophysical Institute, University of Bergen, Norway

Correspondence
Alexander Gohm, Department of Atmospheric and Cryospheric Sciences, University of Innsbruck, Innsbruck, Austria.
Email: alexander.gohm@uibk.ac.at

Funding information
University of Innsbruck's scholarship for studying abroad (KWA)

Abstract

Thule Air Base in northwest Greenland experienced an extreme windstorm during the night of 8/9 March 1972. The event is not among official WMO records because the anemometer broke after recording the highest gust of 93 m s^{-1}. A recent study re-examined the event based on coarse-resolution reanalyses and observations which, however, did not fully resolve the proposed storm processes. This is the first study that uses high-resolution numerical simulations to investigate the processes associated with this windstorm. A cold-frontal inversion and strong flow across the mountain ridge upstream of Thule Air Base (associated with a passing low pressure system) are shown to be key factors for the severe downslope windstorm in the lee of the ridge. It is shown that trapped lee waves occurred during the initial phase of the storm, but did not contribute to the highest wind speeds as proposed in the previous study. It is confirmed that rotor circulations occurred which possibly contributed to the large wind variability and, hence, large differences between individual observation sites. However, no rotors were present at the time of the highest simulated wind speed. Instead, wave breaking above the lee slope is found to indirectly contribute to the wind maxima by facilitating Kelvin–Helmholtz instability at the top of the shooting flow that caused intense wind speed pulsations near the surface. In agreement with the previous study, a corner jet was simulated, however it was not responsible for the strong winds in the vicinity of the air base. Sensitivity experiments showed that the flow field was considerably influenced by the high topography downstream of the air base and that simulations with very thin or no sea ice cover over Baffin Bay resulted in a weaker frontal inversion and up to about 30% lower maximum wind speeds.

KEYWORDS

cold-frontal inversion, downslope windstorm, gravity-wave breaking, rotors, Kelvin–Helmholtz instability, trapped lee waves, WRF model

1 | INTRODUCTION

Wherever fast-moving air encounters mountainous terrain, there is potential for severe weather phenomena such as downslope windstorms. Such phenomena may be manifested in their most extreme forms when strong contrasts in air temperature occur, such as when midlatitude air meets the vast glaciated landscapes and frozen oceans of the polar regions. Due to scarce observational facilities in such areas, presumably many of the most extreme conditions are undetected. Nevertheless, during the night of 8/9 March 1972, a US Air Force base in northwest Greenland, Thule Air Base (TAB), endured and recorded a windstorm that deserves the designation *extreme*. Observed wind gusts reached 93 m s^{-1} at one of the measurement sites at TAB. In a re-examination of this event, Moore (2016) doubted the first explanation of Stansfield (1972) that katabatic flow down the Greenland Ice Sheet and funnelling in local valleys could have produced the observed wind gusts. Rather, Moore (2016) concluded that downslope winds associated with trapped lee waves were responsible for the observed high winds. However, this conclusion was based on reanalyses, surface observations and radiosonde data, i.e. a coarse-resolution dataset that does not fully capture gravity wave processes. Furthermore, the link between trapped lee waves and strong near-surface winds down the lee slope is not obvious. For example, trapped waves might be a concomitant phenomenon but not the direct reason for the strongest winds since the wind speed maximum usually occurs upstream of the first lee wave crest (e.g. Doyle and Durran, 2002; Vosper, 2004). The goal of this study is to explicitly resolve gravity-wave processes with high-resolution numerical simulations and thereby fill the gap in reasoning.

Downslope windstorms, in one form or another, are a well-known phenomenon in many mountainous regions. There have been numerous efforts to theoretically describe such storms during the past century and there has been scientific discussion and dispute about the validity and limitations of different theories. While there were attempts to explain downslope windstorms as a hydraulic analogue of subcritical to supercritical flow transitions (e.g. Long, 1954; Smith, 1985; Durran, 1986; Gohm and Mayr, 2004; Gohm *et al.*, 2008; Jiang, 2014), another branch of theory made the link with reflection and resonance of vertically propagating gravity waves and wave breaking (e.g. Klemp and Lilly, 1975; Peltier and Clark, 1979; Laprise and Peltier, 1989). However, studies of real downslope windstorms demonstrate that in each case different factors can be important and that characteristics can even change throughout individual phases of a single event (e.g. Gohm and Mayr, 2005). Mountain geometry, a temperature inversion close to mountain height, wave breaking above the lee slope of the mountain and vertical layering of wind speed and stability are all factors that have been found to be important with respect to downslope windstorms (e.g. Mayr and Gohm, 2000; Vosper, 2004; Durran, 2015a; Stiperski *et al.*, 2017).

The study area, with TAB at its centre, is shown in Figure 1. Place names were adopted from the Greenlandic geographic information system (NunaGIS, 2018) and previous publications (Stansfield, 1972; Moore, 2016). TAB was built in secret by the US Military starting in 1951 and is located on the south shore of the Wolstenholme Fjord (Figure 1b). The peninsula between Wolstenholme Fjord and Cape York, where TAB is located, does not seem to have its own name and is for the purpose of this study referred to as Pituffik peninsula, after the name of the lowlands upon which TAB was constructed. Pituffik peninsula is the southernmost part of a protrusion on the west coast of Greenland that frames Baffin Bay in the north (Figure 1a). The glacier called Store Landgletscher forms a topographic ridge, southeast of TAB, which is on average 700 m high and rises to join the Greenland Ice Sheet at the connection of the peninsula with mainland Greenland (Figure 1b). If not otherwise specified, *ridge* refers to this specific topographic ridge. The ground around TAB is permafrost and, according to the land use categorization of the ERA-40 reanalysis from the European Centre for Medium-range Weather Forecasts (Uppala *et al.*, 2005), most of the Pituffik peninsula was covered by ice and snow in March 1972.

The study by Moore (2016) has sparked new attention and interest in this historical extreme event by linking the high wind speeds to trapped lee waves, wave breaking, rotors and a corner jet. The goals of this study are

- To use high-resolution numerical simulations to investigate the atmospheric processes that led to the windstorm and observed extreme wind speeds at TAB;
- To test the hypotheses in Moore (2016) against results from the numerical simulations;
- To asses the sensitivity of the model results to varying sea ice and snow cover as well as the influence of mountainous terrain downstream of TAB;
- To compare this event to established downslope windstorm theory.

The remainder of this article is organized as follows. Available observations of the event as well as the numerical model are described in Section 2. In Section 3 results from the numerical simulations are used to describe the synoptic- and mesoscale development before and during the windstorm. This section also contains selected results of the control simulation and two sets of sensitivity experiments that highlight important aspects of the windstorm at TAB. Results are discussed in Section 4 and conclusions are drawn in Section 5.

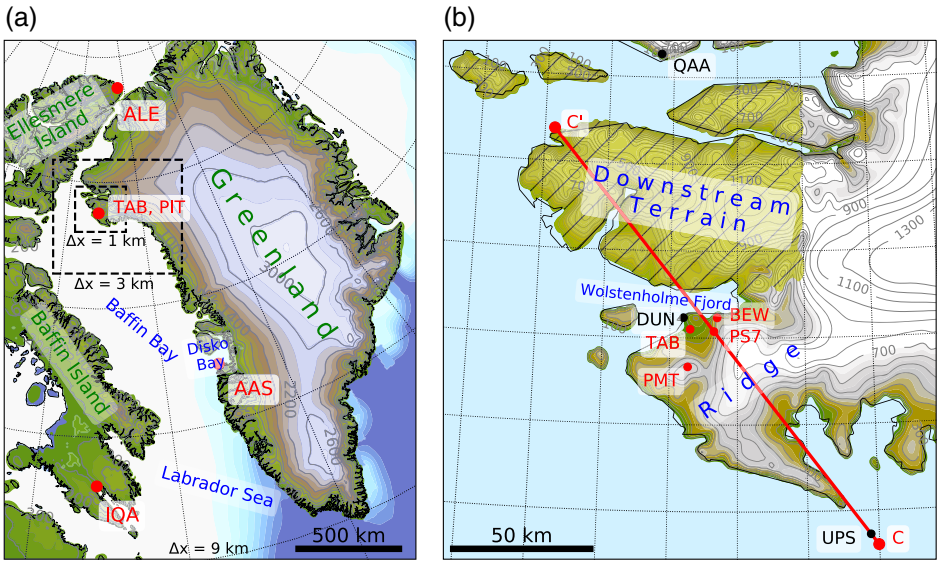

FIGURE 1 (a) Second WRF model domain with $\Delta x = 9$ km, and location of two nested domains (dashed boxes) with $\Delta x = 3$ km and $\Delta x = 1$ km. Sea ice fraction from ERA-40 is indicated from zero (blue) to one (white) and locations of TAB and the radiosonde stations listed in Table 2 are shown in red. (b) Immediate surroundings of TAB inside the $\Delta x = 1$ km domain. Measurement sites TAB, PS7, BEW and PMT from Stansfield (1972) are marked in red. Important geographic features are labelled in blue. The downstream terrain that was flattened in the DFLT simulation is hatched and coloured. The SYNOP stations DUN and QAA as well as the upstream location (UPS) are marked in black and the cross-section line C–C′ is shown in red. Grey contour lines indicate terrain height with increments of (a) 400 m and (b) 100 m. Full names and other details of the measurement sites are listed in Table 2

2 | DATA AND METHOD

2.1 | Observations

Observations of the event are rather scarce and are limited to a few SYNOP and radiosonde observations by the Danish Meteorological Institute (DMI) and the documentation from TAB. In October 1972, seven months after the windstorm, Stansfield (1972) published an article that documented the event as it was recorded at TAB. Most of the measurements, including the ones of the highest wind speeds at Phase Shack 7 (PS7), were taken by the observational system at TAB. The meteorological department at TAB as well as the 557th Weather Wing and the 21st Space Wing of the US Army have been contacted by the first author in order to find out whether the original observations of 8 and 9 March from TAB could be recovered. Unfortunately, at the time of writing, no record of the original observations seems to exist. However, there is no reason to doubt the validity of the observations published in the article by Stansfield (1972). Table 1 provides an overview of wind measurements from the observational system of TAB. Locations of the observational sites are indicated in Figure 1b .

PS7 is a survival shelter and measurement site along the road to the Ballistic Missile Early Warning System (BEW) site. Pingsorssuit Mountain (PMT) describes an elevated radar site south of TAB. In addition to the wind measurements, the minimum sea level pressure in the centre of the low pressure system was estimated to be around 970 hPa. Temperatures at TAB were estimated between –18 and –15 °C during the event and the average temperature of PS7, BEW and PMT was –26 °C. Sustained wind speeds in Table 1 conform with the US standard of 2-min sustained wind reporting.

At the time of the windstorm, radio soundings were conducted twice daily at 0000 UTC and 1200 UTC at a station called Pituffik (PIT, WMO no. 04202) directly at TAB. Vertical profiles from this location and other radio soundings from the west coast of Greenland and the Canadian Arctic were used for model validation in section 3. Radiosonde data were obtained from the Integrated Global Radiosonde Archive (IGRA, 2018).

In 1972 there were two SYNOP stations close to TAB, both of which were operated by the DMI. The station named Dundas (DUN, WMO no. 04200) was in the immediate vicinity of TAB and the other one, Qaanaaq (QAA, WMO no. 04205), about 100 km north of TAB (Figure 1b). While DUN recorded observations at 3-hr intervals between 1200 UTC and 0000 UTC, QAA recorded only twice a day at 1200 UTC and 1800 UTC. No indication of the windstorm is apparent in the QAA record and the DUN dataset lacks the possibly most interesting observation at 0000 UTC 9 March, leaving a data void of 15-hr between 2100 UTC 8 March and 1200 UTC 9 March. The wind record at DUN indicates calm conditions (zero wind speed) during a large proportion of the available SYNOP observations, which seems questionable given a mean wind speed in March of above 3 m s^{-1} (Stansfield, 1972). In addition, no extraordinary weather is indicated at TAB at the time of the windstorm. This differs considerably

TABLE 1 Values of sustained wind speed (2-min averages) that were exceeded during the indicated period on 9 March 1972 and measured peak gusts with their associated times as published in Stansfield (1972). Measurement sites are shown in Figure 1b

Location	Sustained wind speed ($m\,s^{-1}$)	Period	Gust ($m\,s^{-1}$)	Time
TAB	≥ 30	0000 UTC – 0400 UTC	49	0355 UTC
PMT	≥ 51	2330 UTC*– 0700 UTC	72**	—
BEW	≥ 51	0200 UTC – 0500 UTC	65	—
PS7	≥ 62	0100 UTC – 0500 UTC	**93**	0155 UTC

All times are for 9 March, except for * which is for 8 March. **The gust value at PMT was estimated.

TABLE 2 All measurement stations of this study with their abbreviation, elevation above mean sea level (if known), WRF model terrain height, and position. Δx is the grid spacing of the model domain from which the model terrain height and data were retrieved, except for * which was retrieved from the 1 km domain

Location	Abbreviation	Elevation (m)	Model elevation (m)	Latitude (°N)	Longitude (°W)
Air base weather stations			**Δx = 1 km**		
Thule Air Base	TAB	77	115	76.533	68.700
Pingsorssuit Mt	PMT		545	76.401	68.728
Ballistic Missile Early Warning System	BEW		328	76.570	68.300
Phase Shack 7	PS7	302	300	76.523	68.328
DMI SYNOP stations			**Δx = 3 km**		
Dundas	DUN	21	71	76.567	68.800
Qaanaaq	QAA	16	36	77.467	69.217
Radiosonde stations			**Δx = 9 km**		
Pituffik at TAB	PIT	77	65*	76.533	68.750
Alert	ALE	65	47	82.500	62.333
Aasiaat	AAS	43	17	68.708	52.852
Iqualuit	IQA	22	61	63.750	68.550

from the Air Base's own observations at TAB (Table 1), therefore one should be cautious when interpreting these SYNOP datasets. The scarce observations are nevertheless used for model validation in Section 3.2.

2.2 | Numerical model

All numerical simulations in this study were performed with version 3.8.1 of the Polar WRF model, a modified version of the Weather Research and Forecasting (WRF) model optimized for applications in polar regions. Polar WRF has been developed by the Polar Meteorology Group at the Byrd Polar and Climate Research Center of the Ohio State University (Hines and Bromwich, 2008; Bromwich *et al.*, 2009; Hines *et al.*, 2011). Modifications to the standard WRF version 3.8.1 primarily consist of altered snow thermal properties and improved heat flux calculations in the land-surface model as well as specification options for sea ice. Calculations are based on the Advanced Research WRF core (Skamarock *et al.*, 2008). In all numerical simulations, four two-way nested domains with horizontal grid spacing of 27, 9, 3 and 1 km were used. The 27 km domain extends from the northern USA to the North Pole, uses a polar stereographic map projection and was chosen to be large enough to capture the track of the relevant low pressure system over the whole duration of the simulation. The locations of the 9, 3 and 1 km nested domains are shown in Figure 1a, and the extent of the 27 km domain in Figure 2. All domains had 110 vertical model levels with the lowest half-level located at 10 m above the ground. Vertical grid-spacing increased from 20 m at the surface to 500 m at 20 km above mean sea level (MSL), from where it was kept constant until the model top at 10 hPa (or about 30 km MSL). The uppermost 10 km served as a gravity-wave absorbing layer based on Klemp *et al.* (2008). The four model domains were initialized in sequence at 0000 UTC 6 March, 0000 UTC 7 March, 1200 UTC 7 March and 0000 UTC 8 March 1972, respectively, which had the advantage that the nested domains received higher resolution initial and boundary conditions than the coarse reanalysis used to drive the 27 km domain (see below). Computations in each domain started before the low pressure system moved into the respective area to allow for some spin-up time.

In this study WRF was run with the Morrison two-moment microphysics scheme (Morrison *et al.*, 2005),

TABLE 3 Overview of numerical simulations presented in this study

Abbreviation	Description	Sea ice (m)	Snow on sea ice (m)	Modified terrain
CTL	Control run	2.0	0.1	NO
DFLT	Model run with flat downstream topography	2.0	0.1	YES
I10S5	Model run with 1.0 m sea ice and 0.05 m snow on top	1.0	0.05	NO
I5S5	Model run with 0.5 m sea ice and 0.05 m snow on top	0.5	0.05	NO
I1S1	Model run with 0.1 m sea ice and 0.01 m snow on top	0.1	0.01	NO
NOI	Model run without sea ice	0.0	0.0	NO

the Mellor–Yamada–Nakanishi–Niino (MYNN) level-2.5 scheme for the surface and boundary layer (Nakanishi and Niino, 2004), the Noah–MP Land Surface Model (Niu *et al.*, 2011), and the Rapid Radiative Transfer Model for long- and short-wave radiation (Iacono *et al.*, 2008). The Grell–Freitas ensemble scheme was applied to parametrize convection in the 27 km and 9 km domains (Grell and Freitas, 2013), but not in the convection-permitting 3 km and 1 km domains. Physics parametrizations were chosen according to recommendations of previous studies which used Polar WRF (Wagner *et al.*, 2011; Steinhoff *et al.*, 2013), as well as based on the extensive testing of Polar WRF by e.g. Hines and Bromwich (2008) and Hines *et al.* (2015).

For the 27 km domain, initial and boundary conditions were provided at a 6-hr interval by the ERA-40 reanalysis dataset (Uppala *et al.*, 2005). In a comparison of various reanalysis products, Moore (2016) found that the ERA-40 and the Japanese JRA-55 (Ebita *et al.*, 2011) reanalyses represented the vertical structure of the radiosonde profile from TAB at 0000 UTC 8 March and the large-scale development of the relevant low pressure system better than the NCEP reanalysis (Kalnay *et al.*, 1996). JRA-55 was not considered in this study since it lacks some of the required input fields to run WRF. ERA-40 provides an option to retrieve fractional sea ice cover. The same values of sea ice fraction were used in all simulations of this study that included sea ice (Figure 1a). A MODIS-based land-use dataset with 20 categories and 15 s resolution was chosen instead of the default version (MODIS-based 21 categories and 30 s resolution), because the latter seemed to contain unrealistic lake and woody savanna features in the vicinity of TAB.

Unlike for sea ice fraction, there is no gridded dataset available for the thickness of sea ice and snow on ice that goes back to 1972, therefore spatially constant values for those quantities had to be defined. Polar WRF has default thicknesses for sea ice and snow on sea ice that were not used in this study (3 and 0.05 m, respectively; Hines *et al.*, 2015). Considering that most of Baffin Bay and the Labrador Sea is generally ice-free at the end of the summer season (Walsh and Johnson, 1979; Mysak and Manak, 1989; Maslanik *et al.*, 2011), it seems unreasonable to assume sea ice could grow to a mean sea ice thickness of 3 m during one season of growth. Based on the sea ice thickness data of the Global Ice–Ocean Modeling and Assimilation System (GIOMAS) reanalysis (Zhang and Rothrock, 2003) which covers 1979 to the present, an average sea ice thickness of 2 m was chosen instead of the default value for the control (CTL) simulation. The default value for snow depth on top of sea ice, 0.05 m, seems rather low with regard to snow depth measurements from Arctic drift stations (Warren *et al.*, 1999), therefore it was set to 0.1 m in the CTL run. In addition to the CTL simulation with 2 m sea ice and 0.1 m snow on sea ice, a series of sensitivity experiments with different sea ice and snow thicknesses were conducted as well as one sensitivity experiment in which the topography downstream of TAB was modified (all simulations are in Table 3): no sea ice and no snow (NOI), 0.1 m sea ice and 0.01 m of snow (I1S1), 0.5 m sea ice and 0.05 m snow (I5S5), 1 m of sea ice with 0.05 m of snow on top (I10S5), and modified downstream topography (DFLT). Sea surface temperature (SST), which is contained in the ERA-40 dataset, is not updated during the simulations. During the NOI simulation, in the areas where sea ice was removed, SST was constant at the freezing point of sea water, typically 271.46 K. For the DFLT simulation, the WRF topography of the peninsula downstream of TAB (Figure 1b) was flattened to sea level with a smooth transition to normal topography within a buffer zone that was wide enough to avoid exceptionally steep slopes (the surface type, almost exclusively snow and ice, remained unchanged). Table 3 summarizes all simulations performed in this study.

3 | RESULTS

3.1 | Synoptic-scale development

First the large-scale development that led to the downslope windstorm at TAB based on the CTL run is described. The low pressure system which generated the downslope windstorm at TAB formed when two cyclones merged over the Gulf of St. Lawrence, southeast Canada (not shown). The resulting extratropical cyclone crossed the Labrador Sea and by 1200 UTC 7 March 1972, started to interact with the steep topography of south Greenland (Figure 2). While the occluded front was blocked below 3 km and continued along the southeast coast, the centre of the cyclone made landfall on the southwest coast of Greenland. This led to a prefrontal easterly flow across southern Greenland with cloud formation and 3-hr accumulated precipitation of more than 27 mm

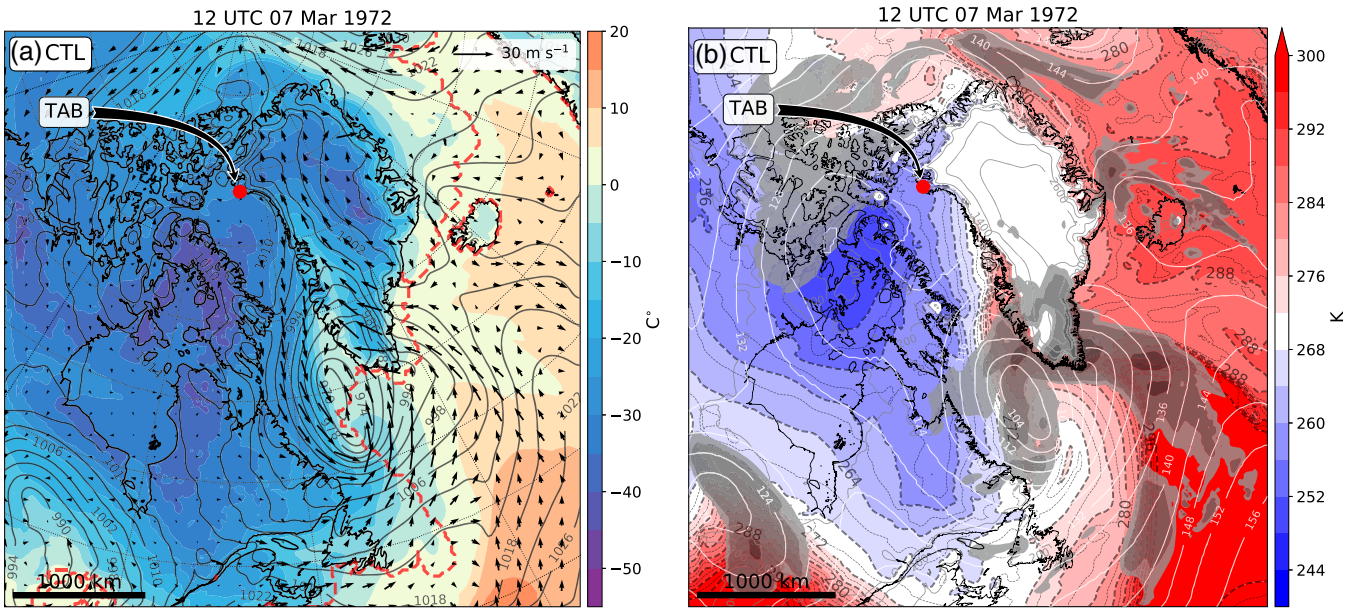

FIGURE 2 CTL simulation (27 km domain) at 1200 UTC 7 March 1972. (a) Sea level pressure (black contours with 4 hPa increments), 2-m air temperature (colour contours with 5 °C increments), and wind field at 10 m AGL (arrows). The red dashed line shows the sea ice edge (fractional sea ice = 0). (b) Equivalent potential temperature (colour contours with 4 K increments, dashed and dotted contours with 2 K increments) and geopotential height (white contours with 4 dam increments) both at 850 hPa, and 3-hr accumulated precipitation (solid and liquid; contours with different grey shades for 0.1–0.5, 0.5–5, >5 mm)

along the steep eastern (windward) slope of Greenland. On the lee side of south Greenland, a dry and relatively warm region developed as a result of terrain-induced adiabatic subsidence (Figure 3a,b). With 52 m s^{-1}, the flow down the western slope of south Greenland was strongest at 2000 UTC 7 March (Figure 3b), where the descending foehn-like flow (Figure 3c) formed a precipitation shadow over a distance of about 600 km in the north–south direction. At 0600 UTC 8 March a distinct closed low pressure centre had reformed over Disko Bay, on the west coast of Greenland (not shown), and subsequently made its way to a position southwest of TAB by 0000 UTC 9 March (Figure 4), providing southeasterly flow in the area around TAB. The reformed cyclone was accompanied by two distinct air mass boundaries. A warm sector preceded the low pressure centre along the west coast and gradually advanced a warm front northwestward (Figure 4a,b) and a cold front followed directly in the wake of the low pressure centre and started to wrap up around it (Figure 4b,d). The warming on the west coast of Greenland prior to the passage of the cold front was partly the result of warm air advection by the cyclone and partly caused by the descending southeasterly flow on the leeward side of Greenland (Figure 3). Near-surface air over Baffin Bay can get very cold in winter due to little insolation and the effect of the sea ice cover, which insulates the atmosphere from the ocean (cf. Figure 2a). It was cold air of this type which the warm front displaced north of the low pressure centre, and which followed in the wake of the cyclone as it approached TAB.

3.2 | Model validation

Radiosonde profiles from the coast of Greenland and Canada at 1200 UTC 8 March 1972 are compared to corresponding profiles of the CTL run in Figure 5a. Figure 5b shows the locations of the radiosonde launch sites superimposed on the potential temperature map for 1200 UTC 8 March for which the radio soundings are valid. For the 27 km model domain, this time corresponds to 60-hr of model integration. Agreement between observations and the model results is satisfactory. This gives confidence that the model results of this study represent in a plausible way the large-scale development as well as the structure of the boundary layer with a near-surface inversion. The potential temperature profiles in Figure 5a reflect the synoptic situation seen in Figure 5b with the southernmost profile, IQA, being the coldest and the troposphere above the low-level inversion becoming warmer at radiosonde sites at higher latitudes (i.e. AAS, followed by PIT and ALE). Below 2.5 km MSL the radiosonde profile from PIT (launched at TAB) was the warmest and featured the sharpest temperature inversion below 1 km. Above 1 km the PIT profile had the smallest vertical gradient of potential temperature and was therefore the least stable.

In addition to radiosonde profiles, surface observations from various SYNOP stations on the west coast of Greenland were compared to the corresponding model time series. Figure 5c shows the comparisons for the two stations nearest to the target area, DUN and QAA (Figure 1b and Table 2 give details). At these two stations the largest differences between model and observations were detected. The discrepancies are

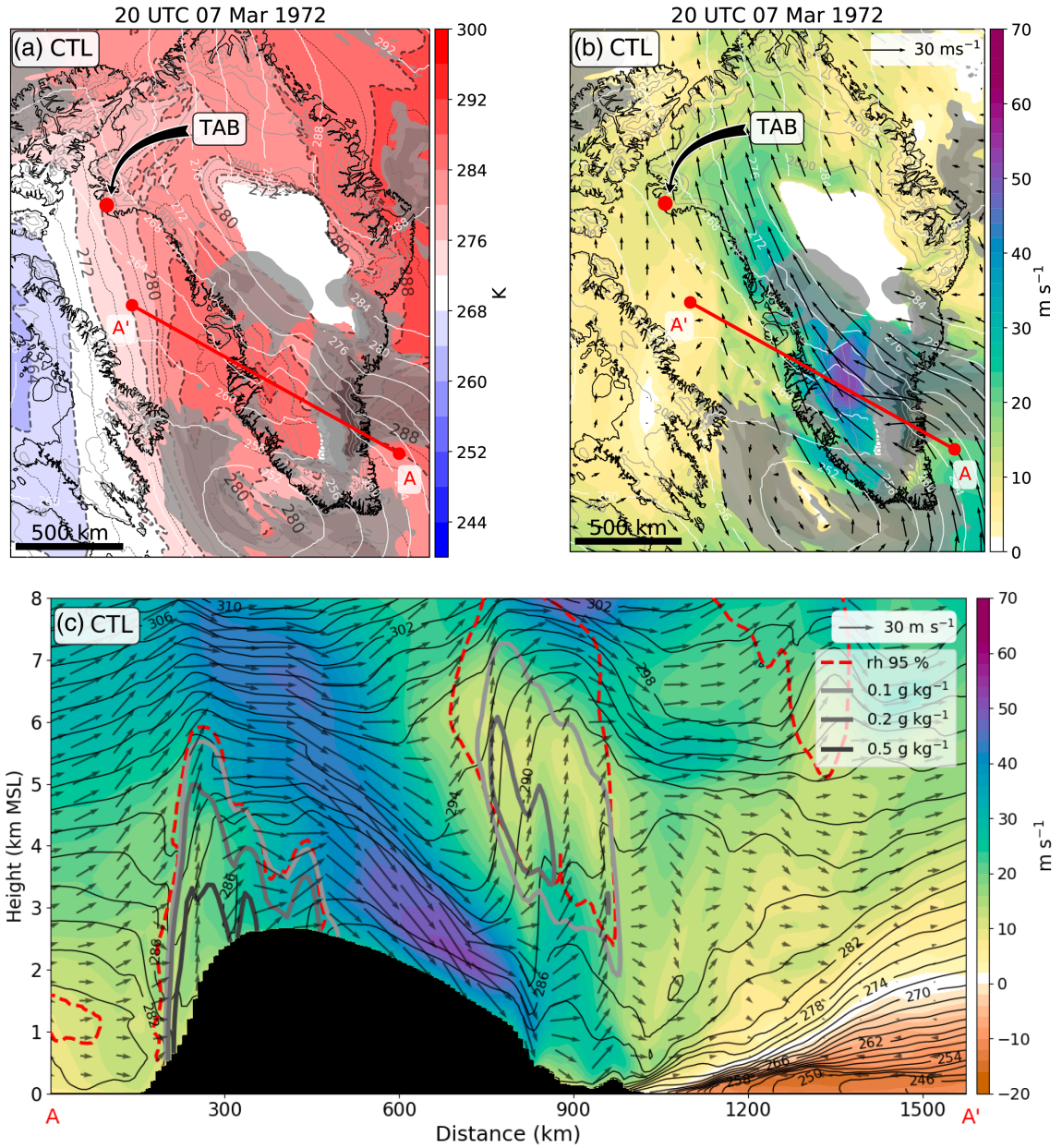

FIGURE 3 CTL simulation (9 km domain) at 2000 UTC 7 March 1972. (a) Equivalent potential temperature (dashed contours with 2 K increments) and geopotential height (white contours with 4 dam increments), both at 700 hPa. (b) Wind speed (colour contours in m s^{-1}), wind vectors (reference vector shown in upper right corner), and 2-hr accumulated precipitation (solid and liquid; contours with different grey shades for 0.1–0.5, 0.5–5, >5 mm). (c) Vertical cross-section along line A–A′ shown in (a) and (b) of transect-parallel wind component and wind vectors, equivalent potential temperature (black contour lines with 2 K increments), total hydrometeor mixing ratio (grey contour lines for 0.1, 0.2 and 0.5 g kg^{-1}) and relative humidity (red dashed contour for 95%)

most apparent in the comparisons of 2-m temperature, 10-m wind and relative humidity (top three and bottom panels in Figure 5c). Figure 5c shows that the 15-hr period of missing observations at DUN between 2100 UTC 8 March and 1200 UTC 9 March, and the 18-hr without observations at QAA were long enough so that the complete period of high winds (cf. Table 1) could have passed unrecorded by the SYNOP stations. As a result, there are no SYNOP observations to validate the model results during the period of the simulated windstorm (grey shaded area in Figure 5c). The time of the windstorm agrees well with the remark in Stansfield (1972) that the storm caused Phase 3 conditions for 15-hr between 2055 UTC 8 March and 1205 UTC 9 March at TAB. Phase 3 is the category for the most severe arctic weather conditions at TAB and results in all air base personnel being restricted to the buildings they are in at the time of declaration. The large differences in 2-m temperatures of up to 19 K between the CTL run and SYNOP observations only partly result from the height difference between model and real topography (Table 2). Comparison of modelled 2-m

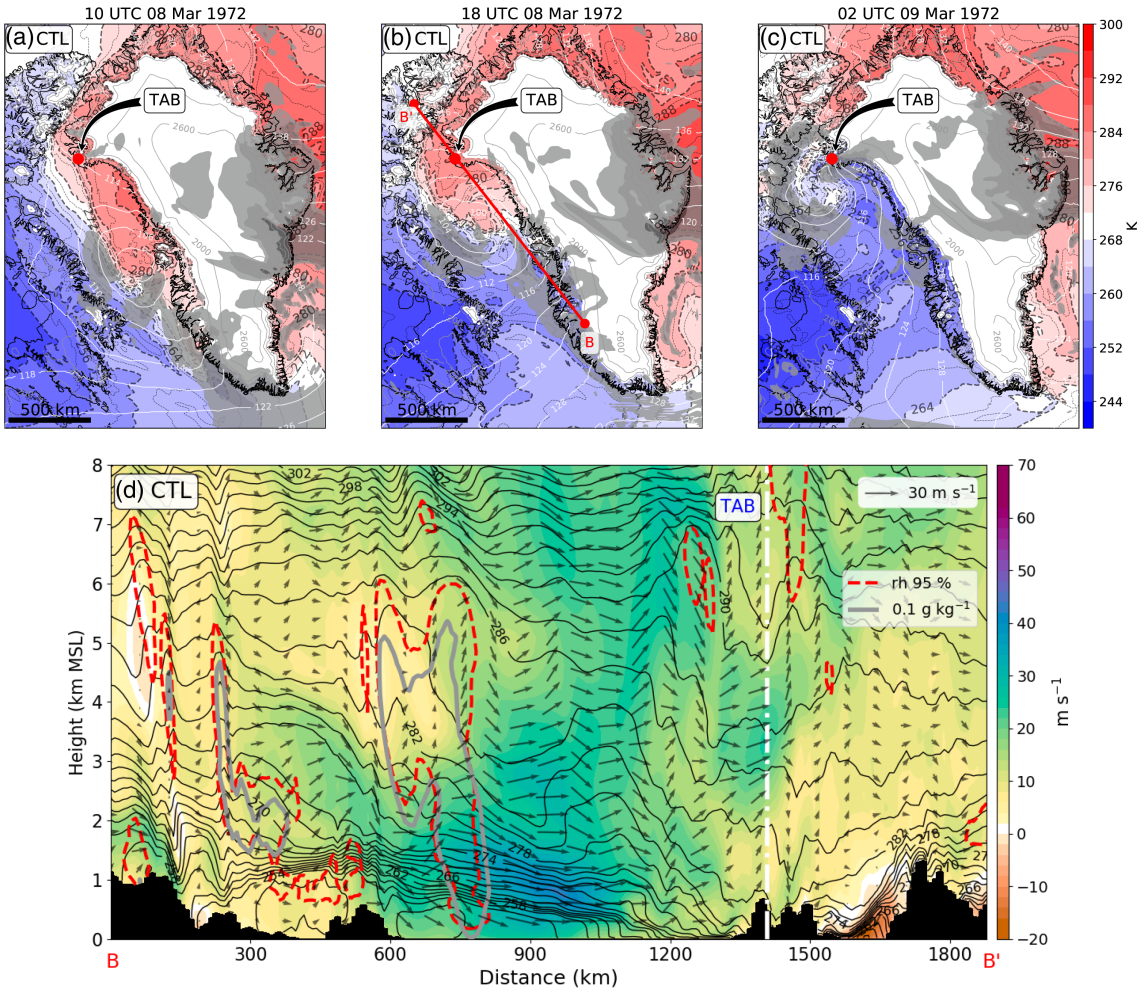

FIGURE 4 (a)–(c) are as Figure 3a, but at 850 hPa. (d) is as Figure 3c but at 1800 UTC 8 March 1972 and along line B–B′ which is indicated in (b)

temperatures of a nearby model grid point at 0 m MSL with DUN yields a similar warm bias of the model at 1800 UTC 8 March (not shown). The difference might rather be connected to a strong near-surface temperature inversion that was present in the Wolstenholme Fjord at 1200 UTC 8 March (PIT profile in Figure 5a) in both the radiosonde observation and the model profile. This inversion is still present in a radiosonde profile from 0000 UTC 9 March that is not shown here (Figure 12a in Moore, 2016). In comparison, the CTL simulation indicates that the near-surface inversion at DUN was eroded and horizontally displaced when the downslope windstorm first reached the bottom of the fjord between 1500 UTC and 2100 UTC 8 March, which resulted in an increase in 2-m temperature and 10-m wind speed and a decrease in relative humidity (Figure 5c). Therefore, air from close to ridge level was adiabatically brought down to DUN, which explains the temperature rise to –1 °C at DUN (cf. potential temperature at PIT of about 272 K between 0.7 km MSL and 1 km MSL in Figure 5a). Most likely this near-surface inversion persisted longer in reality, hence the downslope windstorm penetrated into the valley a few hours later, as supported by strong winds observed after 0000 UTC 9 March (Table 1). However, not all SYNOP observations disagree with model results and especially the development and magnitude of sea level pressure agrees well at all locations and captures the passage of the low pressure system. Model time series in Figure 5c were extracted from the 3 km domain in order to get a longer period for comparison. However, the higher resolution of the 1 km domain did not reduce the model bias at these stations (not shown).

To summarize, the model fails to capture the exact time of the storm onset at TAB, presumably as a result of not being able to correctly represent small-scale turbulent processes at the top of the cold pool in the fjord. However, deficiencies in cold pool processes do not necessarily imply deficiencies in the severity of the storm once the cold pool is eroded (e.g. Zängl *et al.*, 2004). Moreover, the model captures the synoptic evolution of the storm and especially the period and magnitude of the strongest winds at TAB (cf. Table 1 and Figure 5c). Hence, the simulation is suitable for assessing the mesoscale evolution and structure of the downslope windstorm.

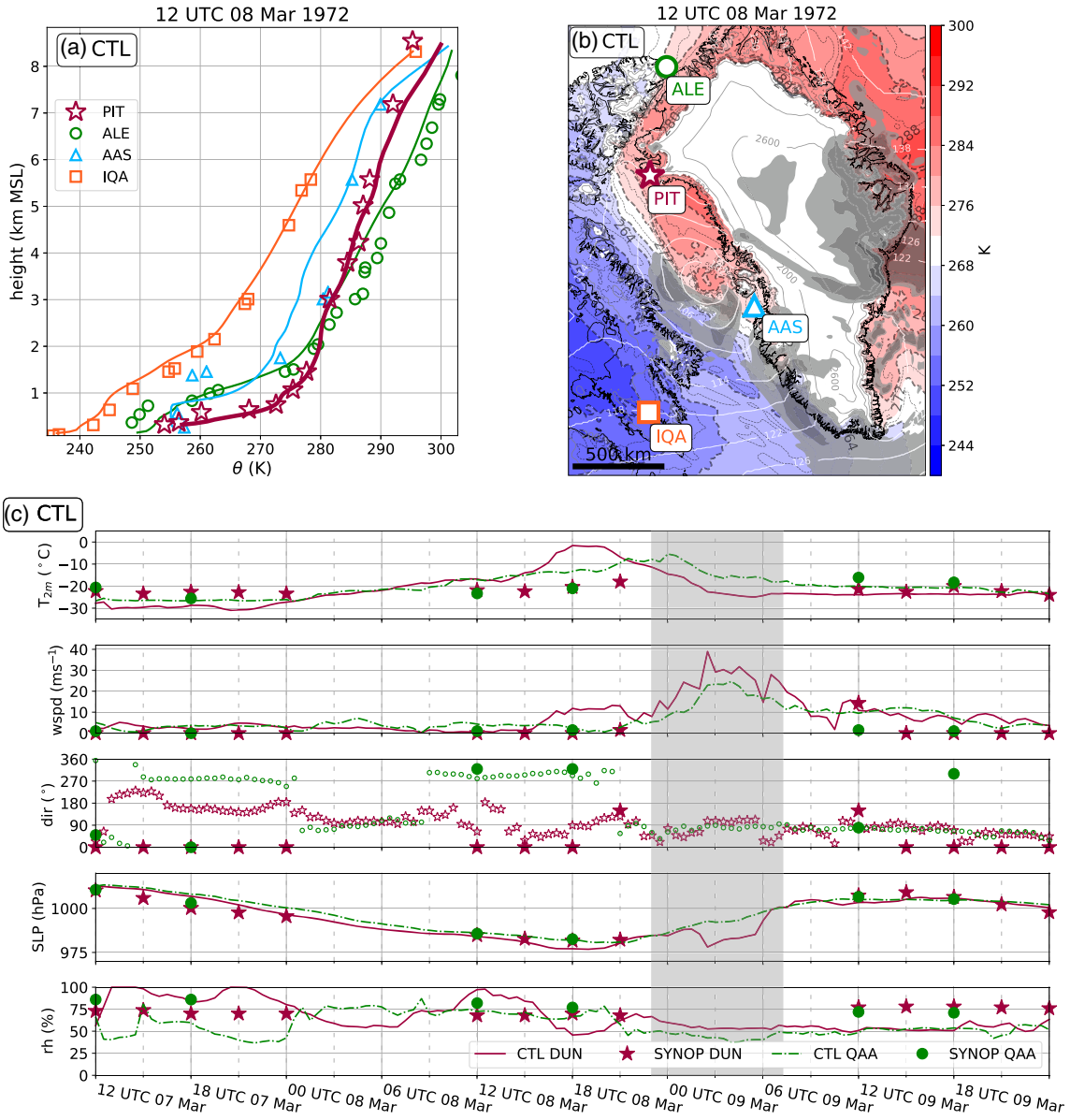

FIGURE 5 (a) Comparison of radiosonde observations of potential temperature with profiles from the 3 km domain of the CTL simulation at 1200 UTC 8 March 1972 at four sites indicated in (b). Solid lines are model profiles, and markers represent observations. (b) is as Figure 4a–c but for 1200 UTC 8 March; markers indicate the locations of radiosonde launch sites. Full names and locations of the launch sites are listed in Table 2. (c) Comparison between SYNOP observations and model time series for the two DMI stations DUN (red) and QAA (green) (locations indicated in Figure 1b). Sea level pressure, 2-m temperature and relative humidity, 10-m wind speed and wind direction are shown. 0 °wind direction together with zero wind speed denote calm conditions. Further details on the stations are given in Table 2. The grey shaded area indicates the period of the windstorm from the CTL run at PS7 (2300 UTC 8 March to 0700 UTC 9 March)

3.3 | Mesoscale evolution and structure

In the early hours of 8 March 1972 at TAB, there was no indication that conditions for a severe windstorm were building up and that only a couple of hours later the area around the air base, particularly PS7, would experience the strongest winds since the beginning of the record in 1951 (Stansfield, 1972). The time–height diagrams in Figure 6 illustrate the evolution of the flow field at UPS and PS7 (i.e. up- and downstream of the ridge; Figure 1b) from 0000 UTC 8 March to 0000 UTC 10 March. The wind component parallel to the transect C–C′ as well as equivalent potential temperature (θ_e) are shown. Figure 7 shows four selected profiles of these quantities at UPS before and during the windstorm (corresponding times are also marked in Figure 6a). At 0120 UTC 8 March the troposphere at UPS and PS7 had a two-layer structure with a very stable layer close to the ground below 0.5 and 1 km MSL, respectively, and the rest of the troposphere above had nearly constant stratification (Figures 6a and 7a). At 0000 UTC 8 March the measured and simulated 2-m temperatures at DUN were –23 and –27 °C, respectively, which is close to the climatological mean temperature for March at TAB (–25 °C;

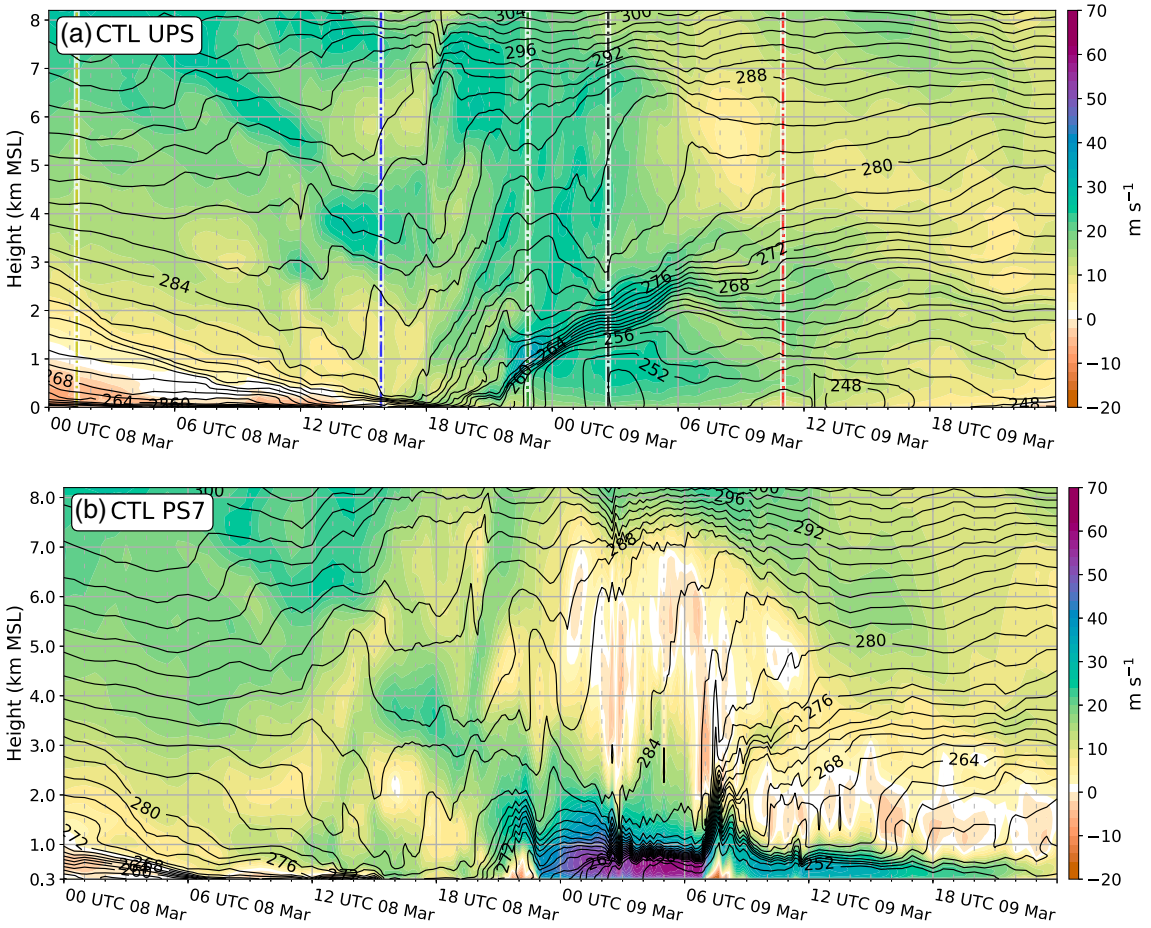

FIGURE 6 Time versus height diagram of the horizontal wind component in the direction of the transect C–C′ indicated in Figure 1b (colour contours in m s^{-1}) and equivalent potential temperature (black contours with 2 K increments) at (a) UPS and (b) PS7. Coloured vertical lines in (a) mark the times of the vertical profiles in Figure 7

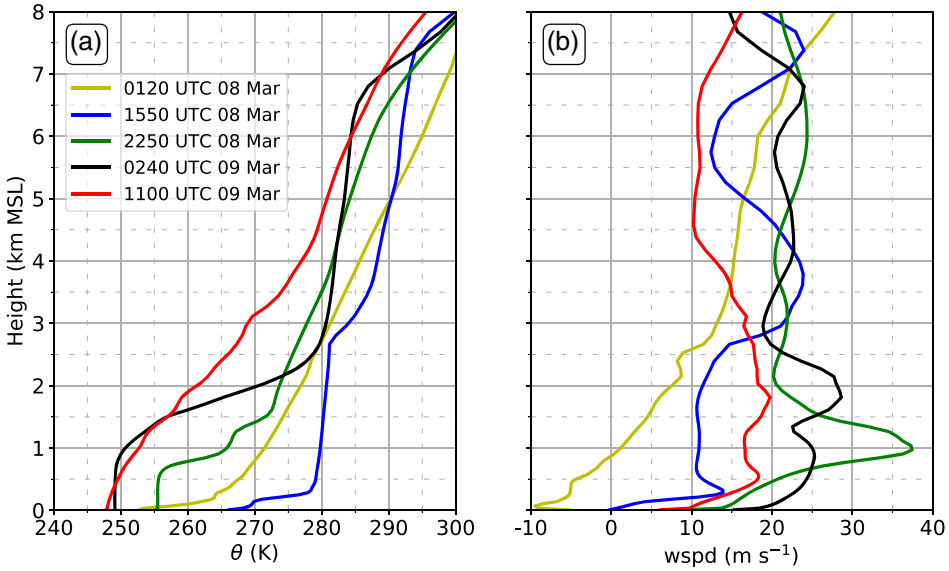

FIGURE 7 Vertical profiles of the CTL simulation at UPS between 8 and 9 March 1972 of (a) of potential temperature and (b) horizontal wind component parallel to the line C–C′. The times were chosen to show the range of conditions before and during the windstorm at UPS and are given in the legend and marked in Figure 6a

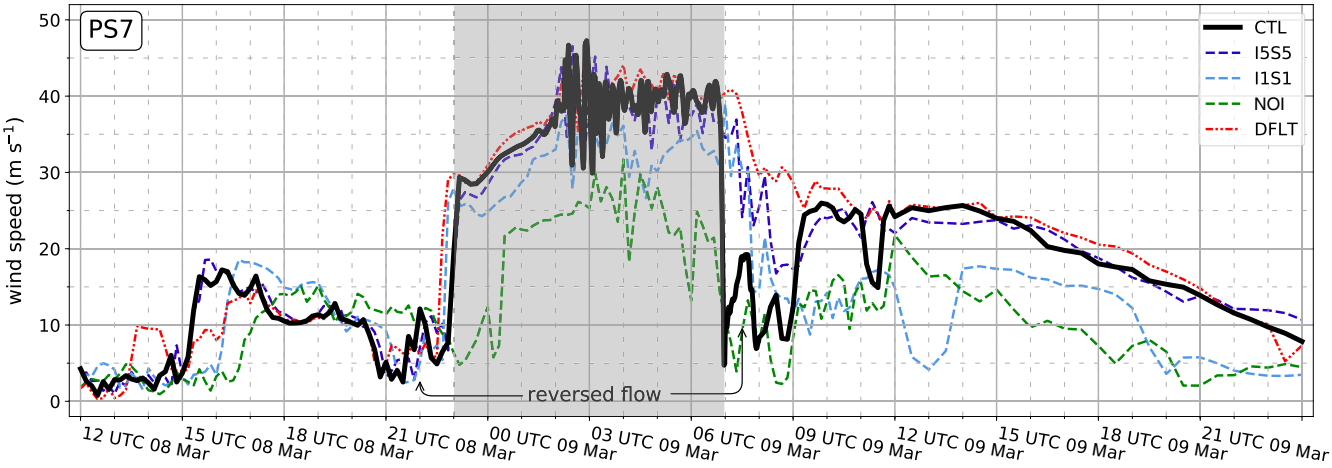

FIGURE 8 Time series of wind speed on the lowest model half-level (10 m AGL) at PS7 (Figure 1b). Shown are the CTL simulation (thick solid black line) and the various sensitivity experiments, DFLT (dotted, red) as well as NOI, I1S1 and I5S5 (dashed, green and shades of blue). The grey shaded area indicates the period of the windstorm from the CTL run at PS7 (2300 UTC 8 March to 0700 UTC 9 March 1972)

Stansfield, 1972). There was a light breeze, 2 m s^{-1}, at DUN (CTL run) and 3 m s^{-1} at PS7 (CTL run; Figure 8).

Until 1550 UTC 8 March, θ_e and θ at UPS and PS7 had been steadily increasing below 4.5 km due to warm air advection by the approaching low pressure system and the associated warm front (Figures 3a,b and 7a). Above 4.5 km, θ had slightly decreased over the same time (Figure 7a). At PS7, which lies at 302 m MSL on the lee slope of the mountain, θ_e already reached a maximum of 282 K shortly after 1500 UTC 8 March. This θ_e maximum came when wind speed at PS7 started to increase with a first advance of the downslope windstorm that eroded and displaced the near-surface inversion on top of the cold pool in the Wolstenholme Fjord (sequential increase in wind speed at PS7 in Figure 8 and at DUN in Figure 5c).

From 1730 UTC 8 March θ_e started to decrease drastically throughout the troposphere at UPS (Figure 6a). This was the result of a cold front that had wrapped around the low pressure centre (Figure 3b,d) and started to push under the warm sector that had formed earlier over Disko Bay and had spread over northwest Baffin Bay (Section 3.1). Figure 9a,b illustrates the flow field at 104 m MSL and along the vertical transect C–C′ at 2200 UTC 8 March. At this time a rotor circulation had established at PS7 (Figures 6b and 9b). Atmospheric rotors are low-level vortices with horizontal axes parallel to the ridge line (Doyle and Durran, 2002), which are typically associated with trapped lee waves and reversed flow near the surface (cf. Figure 9b). Trapped lee waves over the downstream terrain, as seen in Figure 9b between $x = 120$ and 180 km, were present only during this early phase of the windstorm.

By 2250 UTC 8 March, a three-layer structure had developed at UPS with a well-mixed layer below 0.8 km MSL capped by the frontal inversion up to 1.5 km MSL with a shallow jet embedded in the inversion and a less stable layer aloft (green lines in Figures 6a and 7a,b). Due to the upstream tilt, the frontal inversion had lifted about 1 km by 0240 UTC 9 March and the layer above had attained close to neutral stability (black lines in Figure 7a). The three-layer structure that evolved between the two profiles at 2250 UTC 8 March and 0240 UTC 9 March represents the relevant conditions during the main phase of the downslope windstorm (2300 UTC 8 March to 0700 UTC 9 March; grey area in Figure 8). PS7 on the downstream side of the ridge experienced a strong increase in wind speed at 2300 UTC when the downslope windstorm plunged into the Wolstenholme Fjord (Figures 6b and 8). This sudden increase can be explained by a downstream propagation of a hydraulic jump-like feature that was located about 6 km upstream of PS7 (Figure 9b) at 2200 UTC and passed PS7 1-hr later (Figure 8).

Between 0000 and 0200 UTC 9 March there was a steady increase in wind speed at PS7 (Figure 8). This increase began at the same time as gravity waves started to amplify in the upper troposphere. During the most intense phase of the windstorm between 0200 and 0700 UTC 9 March, a shallow jet with a depth of about 700 m was present between the ground and a very stable layer (Figures 6b and 9d). The jet extended from the ridge crest along the lee slope and down to the fjord where it separated from the ground, ascending into a single lee wave over the Wolstenholme Fjord (Figure 9d). This single wave with its narrow updraught zone resembled a hydraulic jump (e.g. Vosper, 2004). Further waves appeared above the downstream terrain. However, they seem to reproduce the shape of the underlying topography in a more pronounced way than the lee waves that are seen in Figure 9b. Further evidence for the occurrence of trapped lee waves in the early stage of the event, which are not purely the result of the underlying terrain, will be provided in Section 3.5.1.

The above-mentioned amplified gravity waves in the upper troposphere started to break at 0130 UTC 9 March. In this

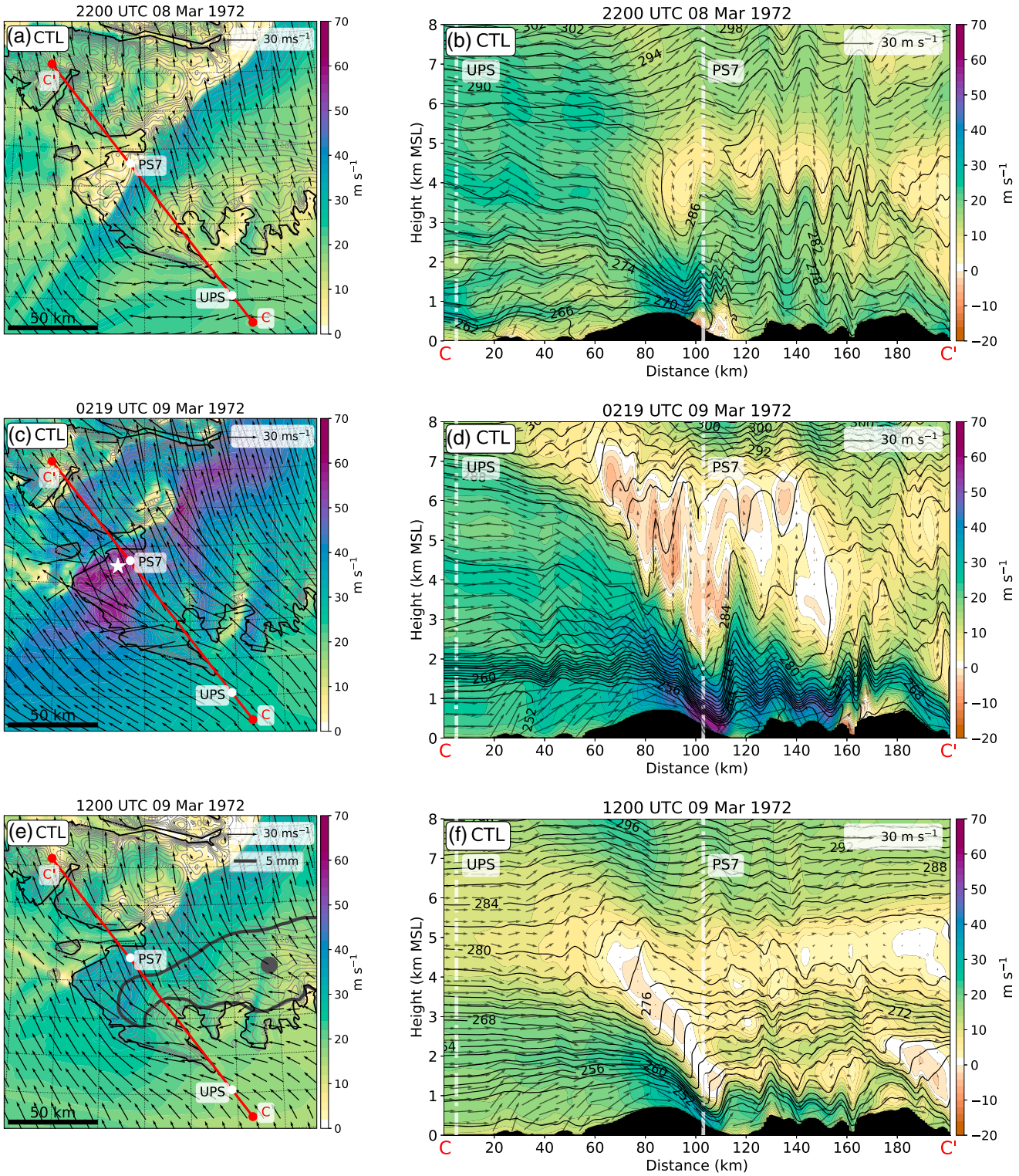

FIGURE 9 Flow field of CTL simulation at (a, b) 2200 UTC 8 March, (c, d) 0219 UTC 9 March, (e, f) 1200 UTC 9 March 1972. (a, c, e) show horizontal wind speed and vectors at 104 m AGL (coloured contours in m s^{-1}). The red line indicates transect C–C′ through PS7 shown in (b, d, f). The wind speed maximum of the CTL run is indicated by the white star in (c). (e) also shows 24-h accumulated precipitation (solid and liquid, bold grey contour), with the maximum 24-h accumulated precipitation at 1200 UTC 9 March (9 mm) indicated by the grey dot. (b, d, f) are as Figure 3c, but for cross-section C–C′ and without relative humidity or hydrometeor mixing ratio. Locations of UPS and PS7 are indicated by white vertical lines

study gravity-wave breaking is diagnosed when overturning isentropes lead to a well-mixed layer with reversed flow above the lee slope (Figure 9d) and high values of turbulent kinetic energy (TKE, not shown). A TKE-based criterion for detecting wave breaking has also been used in other studies (e.g. Bauer *et al.*, 2000). Moreover, a reversed flow is a typical feature of intense wave breaking (e.g. Doyle *et al.*, 2000). Between 0200 UTC and 0300 UTC 9 March, the wave breaking region extended throughout most of the troposphere and reached close to the top of the stable layer, located at about 1 km above ground level (AGL; Figure 9d). During this time, undulations at the top of the stable layer occurred (Figure 10b) and intense wind pulsations appeared at PS7 (Figure 8). At 0219 UTC 9 March, the peak of the simulated downslope windstorm was reached with the highest wind speed of 72 m s^{-1} at 104 m AGL, 9 km west of PS7 (white star in Figure 9c). In comparison, during the real event the anemometer at PS7 observed the highest but last gust of 93 m s^{-1} before the anemometer broke at 0155 UTC. Note that there is a slightly forward tilted, nearly overturning isentrope visible at 5 km MSL in Figure 9b, which is associated with a layer of weak stability advected from the upstream side. However, in this early stage of the storm before about 0100 UTC, isentropes stayed nearly vertical, TKE remained low (not shown) and no upper-level reversed flow formed. Consequently, downslope winds were much weaker before 0100 UTC than afterwards.

At 0400 UTC 9 March a weaker local wind speed maximum occurred offshore, southwest of the Pituffik peninsula at about 0.5 km amsl with winds close to 50 m s^{-1} (not shown). This local maximum collocates with what is referred to as a corner jet in Moore (2016). A corner jet can form on the left and right side of an obstacle (looking in the downstream direction) when the impinging air stream is horizontally deflected by the mountain, resulting in flow around, rather than over, the mountain (Schär and Durran, 1997). In the Northern Hemisphere and for large mountain heights, rotational effects can additionally enhance wind speeds on the left side of the mountain (Thorsteinsson and Sigurdsson, 1996; Doyle and Shapiro, 1999; Barstad and Grønås, 2005).

From about 0600 UTC 9 March, the elevated inversion at 2.5 km MSL lost strength and the θ_e-profile approached continuous stratification at UPS (Figure 6a). At the same time, the flow separation point (i.e. the location where the jet detaches from the surface; Figure 9d at $x = 110$ km) moved further upstream by 20 km. In Figures 6b and 8 the CTL simulation features a strong drop in wind speed when the separation point reached PS7 at about 0700 UTC. The reversed flow close to the ground in Figure 6b at 0700 UTC indicates that there was a rotor circulation present underneath the first trailing lee wave at the end of the shooting flow (further discussed in Section 3.4). After 0700 UTC, when the troposphere above PS7 became more continuously stratified, strong but less severe winds of about 30 m s^{-1} persisted underneath a shallower wave breaking region (Figures 6b and 9e,f), but started to diminish from 1400 UTC 9 March (Figure 8). At 1100 UTC 9 March, the troposphere at UPS had nearly constant stratification throughout (Figure 7a).

There was orographic precipitation mainly over the windward side of the ridge from 2110 UTC 8 March to 0420 UTC 9 March. Figure 9e shows the 24-hr accumulated precipitation at 1200 UTC 9 March with the maximum precipitation sum of 9 mm indicated by a grey dot. Even though some precipitation was carried by the wind to the lee side of the ridge, there was a clear precipitation shadow with 24-hr accumulated precipitation in the CTL run being about ten times lower than that upstream of the ridge.

3.4 | Spatial heterogeneity of the wind field

Even though all measurement stations of the air base's observational system presented in Stansfield (1972) are within a 15 km radius of TAB, observations of sustained wind speed during the storm differ by 32 m s^{-1} and peak gusts by more than 43 m s^{-1} between the four locations (Table 1 and Figure 1b). Judging from the scarce observations that are available, Moore (2016) suggested that these differences could have been caused by the presence of rotor circulations or wave breaking.

The CTL simulation produced multiple rotor circulations both in space and time over the course of the storm. Figure 6b features rotor circulations, represented by reversed flow, before the beginning of the most intense windstorm activity (at PS7, 2300 UTC 8 March; also Figure 9b) and close to the end of it (0700 UTC 9 March; also visible in Figure 10a–c). The spatial and temporal development of the reversed flow is shown in Figure 10c in a distance–time diagram of wind speed at 34 m AGL along the transect D–D′ of Figure 10a (the second model level is shown for better colour distinction). In this transect, reversed flow occurred first at 2100 UTC 8 March, at about 12 km distance from point D (on the ridge line) in Figure 10a. Afterwards, the region of flow reversal shifted downstream along the lee slope and past TAB until 0000 UTC 9 March. In between the occurrence of the main rotor circulations, and especially from 0140 UTC to 0520 UTC 9 March, a rather stationary band of weak line-parallel winds (but only intermittent reversed flow) established close to the coastline. This was the location of the hydraulic jump (also Figure 9d). Near-surface wind in this band was directed across transect D–D′ and out of the Wolstenholme Fjord (between the two periods marked with *rotor* in Figure 10c).

At about 0600 UTC 9 March, a strong rotor circulation reformed underneath the first trailing lee wave and advanced upstream again until 0900 UTC (Figure 10c). The rotor circulation during this time was the strongest of the CTL simulation and reached reversed flow speeds exceeding −20 m/s.

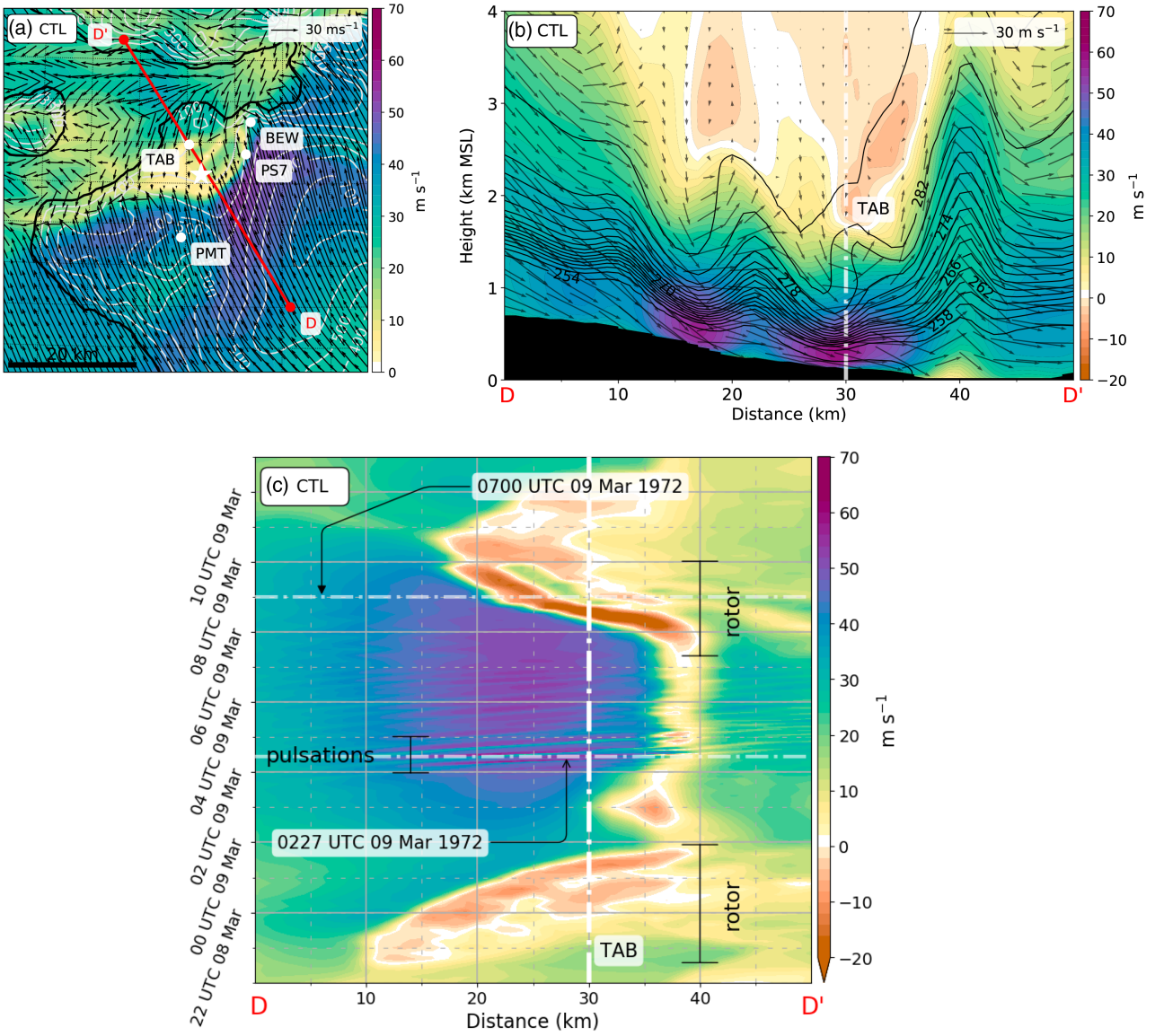

FIGURE 10 (a) Wind speed of the CTL run at 0700 UTC 9 March 1972 on the second model half-level (34 m AGL; colour contours in m s^{-1}), wind vectors (reference vector shown in upper right corner) and terrain elevation contours (grey, 100 m increments). The location of the CTL run's wind speed maximum at 0219 UTC 9 March is indicated by the white star. The transect D–D′ in (b, c) is indicated by the red line. (b) Vertical cross-section of transect-parallel wind component and wind vectors, and equivalent potential temperature (black contour lines with 2 K increments). (c) Transect-parallel wind component on the second model half-level (34 m AGL) against time. The vertical line shows the location of TAB and the horizontal lines indicate the times 0700 and 0227 UTC 9 March shown in (a) and (b), respectively. Periods of wind speed pulsations and rotors are labelled

During both the downslope and subsequent upslope propagation of the main rotor, a second rotor circulation occurred temporarily about 8 km further downstream (e.g. Figures 9b and 10c).

Extensive wave breaking above the ridge (between 2 and 7 km MSL in Figure 9d) and Kelvin–Helmholtz waves at the top of the shooting flow (Figure 10b) coincided with pulsations in the low-level wind speed between 0200 and 0300 UTC 9 March (cf. Figure 10c between 10 and 40 km at the time indicated with *pulsations*). The characteristic period of these pulsations is about 7 to 16 min (Figure 10c). It was at 0219 UTC 9 March during these fluctuations that the highest wind speed of 72 m s^{-1} in the CTL simulation occurred at 104 m AGL.

3.5 | Sensitivity experiments

In addition to the CTL simulation, a series of sensitivity experiments were conducted. First, one simulation was designed to assess the influence of the terrain downstream of TAB on the flow field at TAB. Second, a set of sensitivity simulations with varying sea ice and snow conditions was conducted to determine the impact of uncertainties in the sea

ice conditions on the boundary-layer stratification and hence on the structure and strength of the downslope windstorm.

3.5.1 | The role of downstream terrain

One of the main hypotheses of Moore (2016) was that a trapped lee wave was present during the windstorm and that the observed extreme wind speeds were associated with this trapped lee wave. The use of the term *trapped lee wave* in Moore (2016) is somehow ambiguous since it seems to describe a single internal gravity wave in the lee of a topographic ridge similar to the way *stationary internal gravity wave* is used in Durran (2015a). Evidence for this hypothesis was presented in the form of a radiosonde profile from PIT at 0000 UTC 9 March. It was argued that the perturbation velocity retrieved from the radiosonde profile contained the signature of a surface-trapped wave and that the profiles of potential temperature and wind speed were such that the Scorer parameter, $l \approx N/U$, decreased between the ground and 5 km MSL (Moore, 2016). The latter is a necessary condition for the occurrence of trapped lee waves (e.g. Durran, 2015b). In a two-layer atmosphere, lee waves can only exist if the Scorer parameters, l_L and l_U of the lower and the upper layer, fulfil

$$l_L^2 - l_U^2 > \frac{\pi^2}{4H^2}, \quad (1)$$

with H being the height of the interface (Scorer, 1949). Indeed, such trapped lee waves formed in the CTL simulation together with a rotor underneath the first wave crest, e.g. between about 2000 and 2230 UTC 8 March (Figure 9b). However, they do not necessarily imply a strong downslope windstorm along the lee slope. Gravity waves with varying wavelength and amplitude in the lee of the ridge appear also at later times during the windstorm (Figure 9b,d,f). The shape of some of these waves, especially after 2300 UTC, closely resembles the underlying terrain (e.g. Figure 9d,f), which is why it is unclear to what extent these waves are trapped waves that originate from the primary mountain ridge, and to what degree their position and shape is forced by the local terrain downstream of the main ridge.

Therefore, a sensitivity experiment DFLT was conducted, in which part of the downstream terrain (marked region in Figure 1b) was flattened to sea level while leaving surface characteristics unchanged. Trapped lee waves as in the CTL simulation, shown in Figure 9b, occur in a similar manner in the DFLT run between 2000 and 2230 UTC (not shown). The highest wind speed of the DFLT simulation was 69 m s^{-1} and occurred at 0210 UTC 9 March.

The flow structure close to the time of the highest wind speeds is illustrated in Figure 11b. It shows the same vertical cross-section C–C′ as Figure 9d for the DFLT simulation at 0300 UTC 9 March, i.e. close to the time of the strongest winds. For comparison, the CTL run is shown in Figure 11a. It is obvious that the mountains downstream of the Wolstenholme Fjord play a major role in decelerating the low-level flow near the coast and further downstream. Without these downstream mountains, the shooting flow extends about 30 km further downstream before a hydraulic-jump-like response causes deceleration to weaker flow. Unlike in the CTL run, in the DFLT run there is no quasi-stationary, large-amplitude wave that resembles a hydraulic jump and terminates the shooting flow (cf. Figure 11a,b). Hence, in the CTL run during the time of the strongest winds, this single wave is formed and its position influenced by the downstream terrain rather than by wave trapping. In the DFLT run the jump propagates upstream during the three-layer regime when the height of the elevated inversion layer increases and the stability decreases (not shown). This behaviour is similar to the CTL run. Furthermore, the decrease in severity of the downslope windstorm after about 0600 UTC occurs in both simulations (CTL and DFLT) and is attributed to a change from a three-layer atmosphere to a more continuous stratification with weaker impinging flow (Figure 7). Although wave breaking prevails during this weakening phase, the well-mixed region and the associated reversed flow become shallower and weaker (cf. Figure 9d,f).

Time series of 10-m wind speed at PS7 (Figure 8) are generally very similar for the DFLT and CTL runs except for one main difference, the prominent drop in wind speed between 0700 and 0900 UTC 9 March which occurred in CTL is missing in DFLT. This wind speed drop at PS7 represents reversed flow associated with a rotor circulation which occurred in CTL (Figures 10a,b and 6b) but not in DFTL at this location (not shown). Although rotor circulations underneath trailing lee waves temporarily occur in both simulations (not during the period of the strongest winds), in the DFLT case the reversed flow is weaker and does not propagate as far upstream as PS7.

3.5.2 | The role of sea ice and snow cover

Results from the CTL run feature an elevated inversion on top of a 700 m deep jet during the time of the strongest winds between 2300 UTC 8 March and 0700 UTC 9 March 1972 (Figure 6b). Elevated inversions close to ridge height are often important features of downslope windstorms and the strength of the inversion (i.e. the magnitude of the potential temperature increase) can influence the wave field and the severity of the windstorm (e.g. Vosper, 2004). Sea ice and overlying snow strongly affect the heat exchange between sea and atmosphere. Without sea ice the skin temperature is higher since it is determined by the SST rather than the temperature on top of the layer of sea ice and snow. A higher skin temperature results in a higher sensible heat flux and stronger warming of the boundary layer, which in turn weakens the elevated inversion of the post-frontal cold air. It is hypothesized

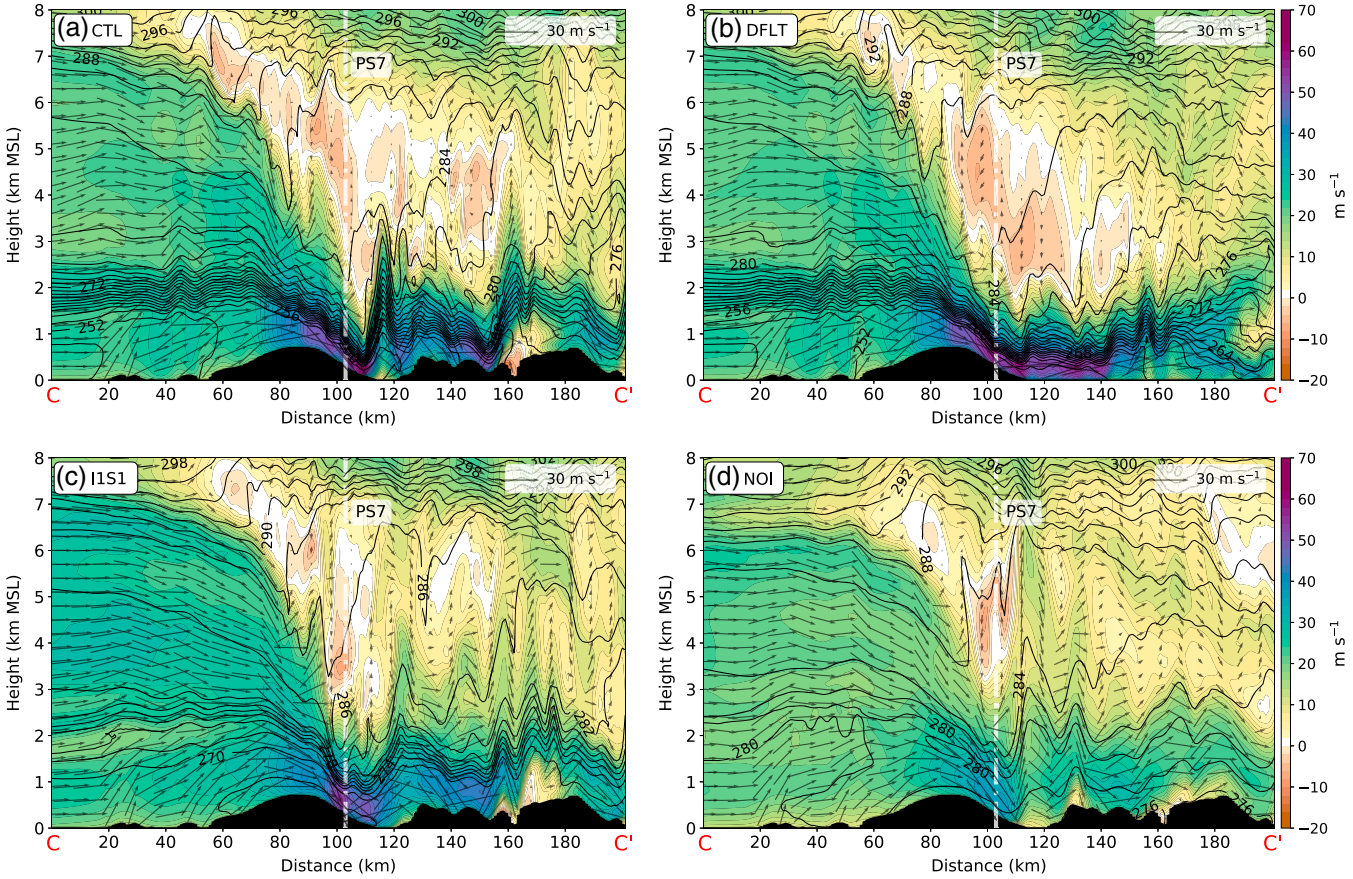

FIGURE 11 As Figure 9b, d, f, but at 0300 UTC 9 March 1972 and for the simulations (a) CTL, (b) DFLT, (c) I1S1 and (d) NOI. The location of PS7 is indicated by a white vertical line

that different thicknesses of sea ice and snow cover affect the θ difference across the stable layer and alter wind strength and wave response of the simulated windstorm. Sea ice and snow thicknesses of the individual sensitivity experiments are listed in Table 3. Effects of snow and sea ice are considered in combination rather than varying the two quantities separately and the sea ice fractions are the same and constant in all experiments with sea ice.

Time series of 10-m wind speed at PS7 of the NOI, I1S1 and I5S5 simulations are shown in Figure 8. Before 1900 UTC 8 March, I1S1 and NOI lag behind CTL by about 1 and 2-hr, respectively, while I5S5 hardly differs from the CTL run during this time. This lag in the early phase of the storm comes from a slightly different development of the cyclone and the way the warm front progresses against the much colder air mass in the CTL run (2-m temperature in the CTL run is prefrontal about 16 K lower than in the NOI run). From 1900 UTC 8 March to 0300 UTC 9 March, only the NOI simulation has different timing while all simulations with sea ice are almost synchronous (Figure 8). After 0300 UTC 9 March, the wind speeds of all sensitivity simulations develop quite similarly, interrupted only by rotor circulations under trailing lee waves that reach PS7 at different times (e.g. CTL at 0700–0900 UTC, and I1S1 at 1200–1400 UTC; Figure 8). Wind speeds during the main period of the windstorm (2300 UTC 8 March to 0700 UTC 9 March) are generally lower for thinner sea ice and snow and lowest with 32% reduced maximum wind speed of 49 m s^{-1} for the simulation with an ice-free ocean, NOI (Figure 8). Uncertainty connected to the thickness of sea ice (2 m) and snow (0.05 m) in the initial conditions does not hugely affect the results, since notable differences between the simulations start to emerge only below an ice thickness of less then 0.5 m.

Simulations with thin sea ice and snow cover or no sea ice showed weaker stable layers during the windstorm. Figure 11a,c,d compare the I1S1 and NOI simulations with the CTL run at 0300 UTC 9 March when the windstorm in these three simulations is at a similar stage of development (cf. Figure 8). While the stratification at UPS above the elevated inversion layer, i.e. above 2.5 km MSL, is affected little by a change in sea ice and snow conditions, the strength of the inversion in the I1S1 and NOI runs is weaker than in the CTL simulation (Figure 11a,c,d). This is due to warmer air in the boundary layer with θ being 20 K (14 K) higher and θ_e being up to 30 K (20 K) higher in the NOI (I1S1) run than in the CTL run. The difference between θ and θ_e values here results from higher moisture in the boundary layer below the capping inversion due to stronger surface latent heat flux especially

over the open sea in the NOI experiment. Consequently, accumulated precipitation over the windward slope of the ridge increases with decreasing sea ice thickness and is about three times more in the NOI run than in the CTL run (not shown).

4 | DISCUSSION

The results presented in Sections 3.1 and 3.3 demonstrate that the local conditions at TAB during the windstorm were closely linked to the synoptic-scale development of a low pressure system and the passage of an associated warm and cold front. More specifically, flow direction and speed as well as the vertical structure at UPS were strongly modified as a result of the passage of the two fronts and mid-tropospheric layers with weak stability (Figures 4, 6a and 7). With the approaching cyclone, TAB was located in the warm sector until the low pressure system had reached a position southwest of TAB and the cold front arrived at UPS with increasing wind speeds. As the upstream tilted frontal inversion was advected over the ridge, a three-layer structure established. The strong frontal inversion acted as an interface that was rising with time between a well-mixed layer below and a weakly stable layer above.

Most of the theories of downslope windstorms and associated gravity waves are based on the steady-state assumption (e.g. Long, 1954; Smith, 1985; Durran, 1986), with a few exceptions (e.g. Hills and Durran, 2012; Menchaca and Durran, 2017). Due to the transient nature of this event, a steady state was never achieved. Nevertheless, parallels with such theories can be found at individual stages of the storm.

Reduced-gravity shallow-water theory has successfully been applied in the past to downslope windstorms (e.g. Gohm and Mayr, 2004; Gohm *et al.*, 2008). However, Jiang (2014) found that this theory is only adequate to describe atmospheric flows in a layer capped by an inversion underneath a deep stratified atmosphere, if the non-dimensional parameters Equations 2 and 3 are both much less than unity,

$$J = N\,U/g' \tag{2}$$

$$\gamma = N\,H_0/\sqrt{g' H_0} \tag{3}$$

where $N = \sqrt{(g/\theta_0)\,(\mathrm{d}\theta_0/\mathrm{d}z)}$ and U are the buoyancy frequency and wind speed in the atmosphere above the inversion, respectively. Further, $g' = g\,\Delta\theta/\theta_0$ is the reduced-gravity acceleration with $\Delta\theta$ being the potential temperature difference across the inversion, θ_0 the potential temperature of the layer below the inversion and H_0 is the depth of the layer below the inversion. The upstream conditions for the most intense phase of the downslope windstorm at PS7 (Figure 9d) exhibit a three-layer structure with an elevated inversion (profiles in Figure 7a between 2250 UTC 8 March and 0240 UTC 9 March). The condition of Jiang (2014) appears to be fulfilled for those two vertical profiles with $J \approx 0.34$ and 0.12, and $\gamma = 0.47$ and 0.36 based on $N = 0.011\,\mathrm{s}^{-1}$ and $0.007\,\mathrm{s}^{-1}$ and $U = 21\,\mathrm{m\,s}^{-1}$ (Figure 7a), respectively. Additionally, the non-dimensional parameter $M_i = N_i\,h_\mathrm{m}/U_0$ is a measure of nonlinearity of the inversion response to the underlying terrain, here N_i is the buoyancy frequency in the inversion, h_m the ridge height and U_0 the base-state wind speed in the lower layer. For the two profiles, $M_\mathrm{i} \approx 1$ and 0.9, respectively. Hence, with J and γ much less than unity and $M_\mathrm{i} < 1.5$, the most intense phase of the storm falls in the so-called *passive category*, which is characterized by a passive layer above the inversion and an inversion that keeps its shape, i.e. does not split downstream of the hydraulic jump (Jiang, 2014). This non-splitting inversion is illustrated in Figure 9d.

The vertical cross-section depicted in Figure 9d exhibits qualitative similarity to a hydraulic flow transition from sub- to supercritical state at the mountain crest, a supercritical shooting flow underneath a region of wave breaking on the leeward side, and a transition back to subcritical flow in a hydraulic jump. According to reduced-gravity single-layer hydraulic theory (e.g. Long, 1954) such a flow transition occurs when the non-dimensional mountain height $M = h_\mathrm{m}/H_0$ exceeds a critical value

$$M_\mathrm{c} = \frac{h_\mathrm{c}}{H_0} = 1 + \frac{1}{2}\,F_0^2 - \frac{3}{2}\,F_0^{2/3}\,, \tag{4}$$

with $F_0 = U_0/\sqrt{g'\,H_0}$ being the upstream Froude number. The three-layer structure seen in Figure 9d (with the separating inversion at H_0 and the potential temperature difference $\Delta\theta$ across the inversion) is suited to calculate a critical mountain height h_c and a critical non-dimensional mountain height $M_\mathrm{c} = h_\mathrm{c}/H_0$. Approximate values for the relevant upstream profiles at 2250 UTC 8 March and 0240 UTC 9 March (Figure 7) are $U \approx 23$ and 22 m/s, $\Delta\theta \approx 16$ and 31 K, $\theta_0 = 256$ and 249 K, and the height of the centre of the inversion layer $H_0 = 1.1$ and 1.7 km, respectively. Hence, $g' = 0.61$ and $1.22\,\mathrm{m\,s}^{-2}$, and $F_0 = 0.89$ and 0.50 for these values. For a typical ridge height $h_\mathrm{m} = 700$ m upstream of TAB, the corresponding non-dimensional mountain heights at these two times are $M = h_\mathrm{m}/H_0 = 0.64$ and 0.43, respectively. According to Equation 4, $M_\mathrm{c} = 0.01$ and 0.19, hence $M > M_\mathrm{c}$ for both times and the regime diagram in Baines (1995, p. 42) suggests a downslope windstorm regime with first a propagating hydraulic jump and later a stationary jump. In the CTL run the hydraulic jump is stationary, however the position seems to be controlled by the downstream terrain (Mayr and Gohm, 2000). Nevertheless, the hydraulic jump propagates further downstream in the DFLT simulation.

Based on a three-layer atmosphere, a well-mixed boundary layer, capped by an inversion and followed by a less stable layer aloft, Vosper (2004) and Sachsperger *et al.* (2017) presented a regime diagram for the $M \times F_0$ space. In this diagram four regimes are distinguished: no lee wave, lee wave,

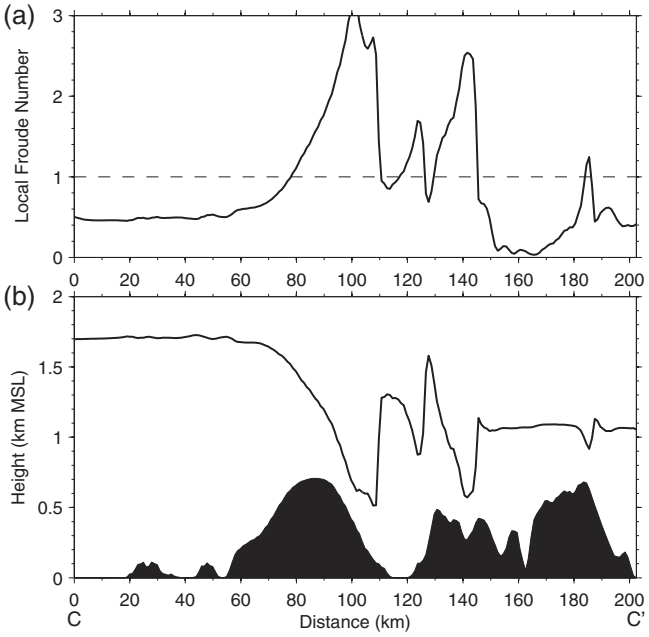

FIGURE 12 Quasi-steady solution of a single-layer shallow-water simulation with final upstream conditions representative for 0240 UTC 9 March 1972. Cross-section C–C′ of (a) local Froude number and (b) layer height together with the terrain height (cf. Figures 9d and 11a)

lee-wave rotor and hydraulic jump. With the above-mentioned pair of values of $(M, F_0) = (0.64, 0.89)$ at 2250 UTC 8 March and (0.43, 0.5) at 0240 UTC 9 March, our case lies in the lee-wave rotor regime, however during the second time period it is close to the hydraulic jump regime.

In order to provide further evidence for the hydraulic response of the flow during the most intense phase of the storm, we performed several simulations with a single-layer shallow-water model (Schär and Smith, 1993). The model was applied in a similar manner as in Gohm and Mayr (2004) and Gohm *et al.* (2008) based on realistic three-dimensional topography. In this case we used the terrain of the 1 km WRF model domain. A quasi-steady state was achieved after about 1-hr of simulation. From the set of simulations with different initial and boundary conditions, we selected the run which matches the upstream conditions at UPS in terms of Froude number (0.5), layer height (1.7 km), and a wind direction (105°) at 0240 UTC 9 March, i.e. close to the time of the strongest winds. Figure 12 shows the corresponding quasi-steady solution. In agreement with the previous Froude number analysis, the initially subcritical flow ($F < 1$) becomes supercritical at the crest ($F > 1$), evolves into a downslope windstorm on the leeward side of the ridge and transitions back into a subcritical flow ($F < 1$) through a stationary hydraulic jump close to the coast (Figure 12a). The behaviour of the shallow-water layer height (Figure 12b) is qualitatively similar to the behaviour of the inversion height in the WRF control simulation (cf. Figures 9d and 11a). The downstream terrain causes another flow acceleration followed by at least three secondary hydraulic jumps similar to the WRF CTL run. A shallow-water sensitivity simulation without downstream terrain (similar to the WRF DFTL run) reveals that the primary hydraulic jump propagates further downstream away from the coast (not shown). This result highlights again the role of the downstream topography in controlling the location of the hydraulic jump and decelerating the flow over the fjord.

In the CTL simulation, trapped lee waves, as seen in Figure 9b, occurred only during a transitional phase between 2000 and 2230 UTC 8 March. During this phase, stability increased in the lower troposphere after the cold front arrived and a weakly stable layer passed between 4 and 6 km MSL. This weakly stable layer led to a minimum in the Scorer parameter even though wind speed at this height was low as well. Scorer parameters in the weakly stable layer, $l_U \approx N_U/U_U = 4.9 \times 10^{-4}\,\mathrm{m}^{-1}$, and in the layer below, $l_L \approx N_L/U_L = 8.7 \times 10^{-4}\,\mathrm{m}^{-1}$, from close to PS7 at 2130 UTC 8 March, fulfil the condition (Equation 1) (Scorer, 1949) with $H = 4$ km for lee wave trapping in a two-layer atmosphere. In comparison to the CTL run, the DFLT simulation yielded very similar trapped lee waves between 2000 UTC and 2230 UTC 8 March. Therefore, it is clear that these waves were virtually independent of the downstream topography. However, in both simulations trapped lee waves occurred at a time when wind speeds at PS7 were rather low or a rotor circulation was present (e.g. Figure 8). Trapped lee waves ceased and the weakly stable layer seen in Figure 9b passed before wind speed increased drastically at about 2300 UTC. Therefore, both simulations suggest that trapped lee waves did not contribute to the highest observed wind speeds at PS7 as was suggested by Moore (2016).

Reversed flow associated with rotor circulations underneath the first of the trailing lee waves occurred in the CTL run (negative wind speed in Figure 10c) and in the DFLT run (not shown) in a very similar fashion between 2000 UTC and 0000 UTC. The second period of intense reversed flow of the CTL run between 0630 UTC and 0800 UTC 9 March was associated with a rotor circulation underneath the large-amplitude wave which was controlled by the downstream terrain. This wave was not present in the DFLT simulation, hence no such intense rotor occurred in the DFLT run. Thus, model results support the hypothesis of Moore (2016) that rotors were present and contributed to spatial variability of the wind field. However, rotors did not have a major influence on the highest winds, since maximum reversed flow speed was about a factor four smaller than the maximum wind speed in the main flow direction. In addition, reversed flow was weak or completely absent during the time of the highest winds at PS7.

The highest wind speed of about 72 m s^{-1} at 104 m AGL occurred on the leeward side of the ridge at 0219 UTC 9

March (white star in Figure 9c) during a short phase of intense pulsations of the near-surface wind field between 0200 and 0300 UTC (Figure 10c). These pulsations started shortly after the vertical profiles of the gradient Richardson number $R_i = N^2 (du/dz)^{-2}$ fell below the critical value of 0.25 at 2.5 km MSL for the first time at 0150 UTC at TAB and PS7. This level is approximately the height of the boundary between top of the stratified shooting flow with large vertical wind shear and the wave breaking region with weak stratification (cf. Figure 9d). The low gradient Richardson number triggered Kelvin–Helmholtz instability (cf. Figure 10b) which is known to cause wind-speed pulses in the shooting flow with typical periods of, e.g. 5 min (Smith, 1991), 7 min (Belušić *et al.*, 2007) and 20 min (Scinocca and Peltier, 1989; Peltier and Scinocca, 1990). A spectral analysis (Welch, 1967) together with a visual inspection of the time series of near-surface wind speed (1 min output of CTL run) close to PS7 between 0200 and 0500 UTC 9 March (cf. Figure 10c) yield pulsation periods between 7 and 16 min. These values compare well with the range of pulsation periods found in the previous studies mentioned above.

Between 2250 UTC 8 March and 0240 UTC 9 March stratification at UPS changes from a sharp and shallow elevated inversion towards a rather deep (1.5 km) separating layer (Figures 6a and 7). Hence, in the latter case, a comparison to the numerical experiments of a two-layer flow by Durran (1986) might be more appropriate. In these experiments the buoyancy frequency in the lower layer N_L was 2.5 times higher than in the upper layer N_U, whereas the background wind speed U was the same. Hence, the Scorer parameter, $l \approx N/U$ (Scorer, 1949), decreased with height which favoured the development of trapped lee waves and rotors (also Doyle and Durran, 2002). By increasing the height of the layer interface H_0 from U/N_L to $4\,U/N_L$, the flow was found to transition from an everywhere-supercritical flow ($H_0 = U/N_L$) to a propagating hydraulic jump ($H_0 = 2.5\,U/N_L$) and via a stationary jump ($H_0 = 3.5\,U/N_L$) to an everywhere-subcritical flow ($H_0 = 4\,U/N_L$) (Figure 5 in Durran, 1986). For most of the simulated windstorm, the flow recovers from supercritical to subcritical flow in a hydraulic jump which is controlled by the downstream terrain, as seen in Figures 9d and 11a at $x = 110$ km distance. Without the downstream terrain (Figure 11b), the position of the hydraulic jump develops in a qualitatively similar manner to the results of Durran (1986) for a rising interface. Hence, first the hydraulic jump propagates downstream, then, with the rising interface, it becomes stationary close to the mountain. Based on the profile from 0240 UTC 9 March in Figure 7a, we calculate $H_0 = 2807$ m, $N_L = 0.021\,s^{-1}$ and $N_U = 0.007\,s^{-1}$, and $U = 23.8\,m\,s^{-1}$. This yields $H_0 = 2.5\,U/N_L$, which is the value for the propagating hydraulic jump solution shown in Durran (1986).

Between 0240 and 1100 UTC 9 March, the stable layer in the potential temperature profile at UPS (Figure 7a) got deeper but less stable until nearly constant stratification was reached (cf. Figure 6a). As the impinging flow got weaker and stratification became more continuous, the hydraulic-jump-like wave over the Wolstenholme Fjord propagated upstream and upslope from 0600 UTC and established a rotor circulation underneath (Figure 10c). At 0730 UTC the wave steepened, broke and formed a persistent turbulent region above the mountain ridge (still seen at 1200 UTC 9 March in Figure 9f between 0.8 and 5 km MSL). A weaker but still strong downslope windstorm persisted underneath this wave breaking region for the rest of 9 March (cf. Figures 6a,b and 8) until it disappeared early on 10 March.

Based on the simplified wind gust estimate method developed by Brasseur (2001) and applied by Belušić and Klaić (2004) in a case of Croatian bora, the magnitude of maximum wind speed within the windstorm layer is an estimate for the maximum wind gust at the surface. Therefore, the simulated maximum of $72\,m\,s^{-1}$ at 104 m MSL at 0219 UTC 9 March of the CTL run can be compared to the observed wind gust of $93\,m\,s^{-1}$ at PS7. Belušić and Klaić (2004) conclude that the biases of simulated wind speeds and estimated wind gusts are proportional. Hence, the underestimated wind gust in our case might be caused by an under-represented mean intensity of the storm. However, capturing the maximum wind speed of the downslope windstorm is generally challenging due to limited predictability of the storm intensity (Doyle and Reynolds, 2008; Reinecke and Durran, 2009).

Weakly stable layers which result from differential diabatic heating associated with fronts and orographic precipitation have impacted the wave field in downslope windstorm events in Norway and the European Alps, as demonstrated by Doyle and Shapiro (2000) and Doyle and Smith (2003). The most intense wave breaking above the lee slope near TAB, which coincided with the pulsations in the surface-near wind field (Section 3.4), started at 0130 UTC 9 March at 6 km MSL. Before that, more continuous stratification above the ridge had followed the passage of a layer with weak stability. Gravity waves that previously were trapped until 2300 UTC 8 March (Figure 9b), were then able to propagate to higher altitudes, amplify and initiate wave breaking. The transient layers of weak stability in Figure 6a most likely originate from gravity-wave breaking as the large-scale easterly flow passed south Greenland as well as from frontal processes (Section 3.1). In our case, in contrast to Doyle and Smith (2003), these layers of weak stability did not result from diabatic processes associated with orographic precipitation directly upstream of the mountain ridge. Clouds and precipitation from orographic lifting on the windward side of the ridge (cf. Figure 9e) were confined below the top of the inversion layer (2–3 km MSL) in all our simulations and could therefore not have caused the layers of weak stability above.

In Moore (2016), it was argued that during the downslope windstorm event a corner jet was present southwest of the Pituffik peninsula and that it contributed to the high wind speeds during the event. The CTL simulation confirms the presence of a local maximum in wind speed southwest of the Pituffik peninsula during the windstorm at about 0.5 km MSL which was strongest (>50 m s^{-1}) at 0400 UTC 9 March (not shown). However, a relation to the highest simulated wind speed that occurred on the leeward side of the ridge at 0219 UTC 9 March (white star in Figure 9c) cannot be confirmed.

Numerical simulations of mesoscale phenomena such as internal gravity wave breaking and downslope windstorms are challenging, as highlighted in the case-study by Doyle and Shapiro (2000). Furthermore, a model intercomparison study by Doyle *et al.* (2011) demonstrated that results from such simulations can vary considerably between different models. Ensemble predictions by Doyle and Reynolds (2008) showed that regime transitions in particular (e.g. from mountain wave to wave breaking regime) are prone to rapid perturbation growth which limits the predictability of such events. Reinecke and Durran (2009) found that predictability varies between different types of downslope windstorms. Nevertheless, in this case the numerical simulations provided valuable indications of the controlling mechanisms of the severe downslope windstorm.

5 | CONCLUSIONS

The mechanisms behind an extreme windstorm event during the night from 8 to 9 March 1972 at Thule Air Base (TAB) in northwest Greenland have been studied based on high-resolution numerical simulations. The aim was to identify the atmospheric processes that produced the observed wind gusts of up to 93 m s^{-1} and to compare results from numerical simulations to the studies of Stansfield (1972) and Moore (2016) which were solely based on observations and coarse-resolution reanalyses. The key findings are:

- A low pressure system passed southwest of TAB and caused strong southeasterly flow over a 700 m high mountain ridge. The passage of the associated warm front and subsequent cold front led to rapid changes in atmospheric stratification which induced different regimes of downslope windstorm near TAB. At the time of the strongest winds (in the CTL run at PS7 between 2300 UTC 8 March and 0700 UTC 9 March 1972), the cold-frontal inversion acted as a density interface that rose in time due to the sloping front and caused a hydraulic flow response with a supercritical shooting flow down the lee side of the ridge towards TAB.
- Vertically propagating gravity waves amplified and overturned above the mountain ridge leading to a highly turbulent wave-breaking region above the capping inversion of the shooting flow. Near the top of this inversion, Kelvin–Helmholtz instability occurred which led to pulsations in the near-surface wind speed with a period of about 7 to 16 min. During this phase of pulsations, the highest simulated wind speed of 72 m s^{-1} occurred underneath the trough of a breaking Kelvin–Helmholtz wave at 104 m AGL, 9 km west of the location where the peak gust of 93 m s^{-1}, was measured during the real windstorm before the anemometer broke.
- Sensitivity experiments with thin or no sea ice and snow cover reduced low-level stratification which resulted in a downslope windstorm that was about 30% weaker. A further sensitivity experiment with flattened terrain downstream of TAB revealed that the extent of the shooting flow as well as the location and amplitude of a hydraulic jump and lee waves were controlled by the downstream terrain.
- Rotor circulation underneath a first trailing lee wave and a hydraulic jump – both occurring at different times – were confirmed to cause large differences in surface wind measurements at different stations in the vicinity of TAB. However, contrary to the hypothesis of Moore (2016), neither a trapped lee wave nor a corner jet was directly responsible for the highest simulated winds at TAB.

This study demonstrates that historical extreme events can be studied by dynamical downscaling of coarse-resolution reanalyses such as ERA-40. However, this work also illustrates that simulations with horizontal grid sizes of $\mathcal{O}$(1 km) have difficulties in correctly representing boundary-layer processes over complex terrain, such as the interaction between the downslope windstorm and the cold pool. The questions of how unusual the development of the low pressure system was, and how exactly the interaction with south Greenland affected this development, remain open.

ACKNOWLEDGEMENTS

The computational results presented here have been achieved using the HPC infrastructure LEO of the University of Innsbruck. Mathias Tollinger was supported by a KWA scholarship of the University of Innsbruck to allow study abroad. We thank John Cappelen from the Danish Meteorological Institute and G.W. Kent Moore from the University of Toronto for providing observational data for the event. We are grateful to three anonymous reviewers whose comments improved this article and for the effort of a proofreader.

ORCID

Mathias Tollinger http://orcid.org/0000-0002-1217-8127
Alexander Gohm http://orcid.org/0000-0003-4505-585X

REFERENCES

Baines, P.G. (1995) *Topographic Effects in Stratified Flows*. Cambridge University Press, Cambridge, UK.

Barstad, I. and Grønås, S. (2005) Southwesterly flows over southern Norway – mesoscale sensitivity to large-scale wind direction and speed. *Tellus A*, 57, 136–152. https://doi.org/10.3402/tellusa.v57i2.14627.

Bauer, M.H., Mayr, G.J., Vergeiner, I. and Pichler, H. (2000) Strongly nonlinear flow over and around a three-dimensional mountain as a function of the horizontal aspect ratio. *Journal of the Atmospheric Sciences*, 57, 3971–3991. https://doi.org/10.1175/1520-0469(2001)058<3971:SNFOAA>2.0.CO;2.

Belušić, D. and Klaić, Z.B. (2004) Estimation of bora wind gusts using a limited-area model. *Tellus A*, 56, 296–307. https://doi.org/10.3402/tellusa.v56i4.14425.

Belušić, D., Žagar, M. and Grisogono, B. (2007) Numerical simulation of pulsations in the bora wind. *Quarterly Journal of the Royal Meteorological Society*, 133, 1371–1388. https://doi.org/10.1002/qj.129.

Brasseur, O. (2001) Development and application of a physical approach to estimating wind gusts. *Monthly Weather Review*, 129, 5–25. https://doi.org/10.1175/1520-0493(2001)129<0005:DAAOAP>2.0.CO;2.

Bromwich, D.H., Hines, K.M. and Bai, L.-S. (2009) Development and testing of Polar Weather Research and Forecasting Model: 2. Arctic Ocean. *Journal of Geophysical Research: Atmospheres*, 114. https://doi.org/10.1029/2008JD010300.

Doyle, J.D., Durran, D.R., Chen, C., Colle, B.A., Georgelin, M., Grubisic, V., Hsu, W.R., Huang, C.Y., Landau, D., Lin, Y.L., Poulos, G.S., Sun, W.Y., Weber, D.B., Wurtele, M.G. and Xue, M. (2000) An intercomparison of model-predicted wave breaking for the 11 January 1972 Boulder windstorm. *Monthly Weather Review*, 128, 901–914. https://doi.org/10.1175/1520-0493(2000)128<0901:AIOMPW>2.0.CO;2.

Doyle, J.D. and Shapiro, M.A. (2000) A multi-scale simulation of an extreme downslope windstorm over complex topography. *Meteorology and Atmospheric Physics*, 74, 83–101. https://doi.org/10.1007/s007030070027.

Doyle, J.D. and Durran, D.R. (2002) The dynamics of mountain-wave-induced rotors. *Journal of the Atmospheric Sciences*, 59, 186–201. https://doi.org/10.1175/1520-0469(2002)059<0186:TDOMWI>2.0.CO;2.

Doyle, J.D., Gaberšek, S., Jiang, Q., Bernardet, L., Brown, J.M., Dörnbrack, A., Filaus, E., Grubišić, V., Kirshbaum, D.J., Knoth, O., Koch, S., Schmidli, J., Stiperski, I., Vosper, S.B. and Zhong, S. (2011) An intercomparison of T-REX mountain-wave simulations and implications for mesoscale predictability. *Monthly Weather Review*, 139, 2811–2831. https://doi.org/10.1175/MWR-D-10-05042.1.

Doyle, J.D. and Reynolds, C.A. (2008) Implications of regime transitions for mountain-wave-breaking predictability. *Monthly Weather Review*, 136, 5211–5223. https://doi.org/10.1175/2008MWR2554.1.

Doyle, J.D. and Shapiro, M.A. (1999) Flow response to large-scale topography: the Greenland tip jet. *Tellus A*, 51, 728–748. https://doi.org/10.1034/j.1600-0870.1996.00014.x.

Doyle, J.D. and Smith, R.B. (2003) Mountain waves over the Hohe Tauern: influence of upstream diabatic effects. *Quarterly Journal of the Royal Meteorological Society*, 129, 799–823. https://doi.org/10.1256/qj.01.205.

Durran, D.R. (2015a) Mountain meteorology; downslope winds, in *Encyclopedia of Atmospheric Sciences*, 2nd edition, North, G.R., Pyle, J., Zhang, F. (eds), Elsevier, Amsterdam, Netherlands, pp. 69–74. https://doi.org/10.1016/B978-0-12-382225-3.00288-7.

Durran, D.R. (2015b) Mountain meteorology; lee waves and mountain waves, in *Encyclopedia of Atmospheric Sciences*, 2nd edition, North, G.R., Pyle, J., Zhang, F. (eds), Elsevier, Amsterdam, Netherlands, pp. 95–102. https://doi.org/10.1016/B978-0-12-382225-3.00202-4.

Durran, D.R. (1986) Another look at downslope windstorms. Part I: the development of analogs to supercritical flow in an infinitely deep, continuously stratified fluid. *Journal of the Atmospheric Sciences*, 43, 2527–2543. https://doi.org/10.1175/1520-0469(1986)043<2527:ALADWP>2.0.CO;2.

Ebita, A., Kobayashi, S., Ota, Y., Moriya, M., Kumabe, R., Onogi, K., Harada, Y., Yasui, S., Miyaoka, K., Takahashi, K., Kamahori, H., Kobayashi, C., Endo, H., Soma, M., Oikawa, Y. and Ishimizu, T. (2011) The Japanese 55-year reanalysis JRA-55: an interim report. *Solaiat*, 7, 149–152. https://doi.org/10.2151/sola.2011-038.

Gohm, A. and Mayr, G.J. (2004) Hydraulic aspects of föhn winds in an alpine valley. *Quarterly Journal of the Royal Meteorological Society*, 130, 449–480. https://doi.org/10.1256/qj.03.28.

Gohm, A. and Mayr, G.J. (2005) Numerical and observational case-study of a deep Adriatic bora. *Quarterly Journal of the Royal Meteorological Society*, 131, 1363–1392. https://doi.org/10.1256/qj.04.82.

Gohm, A., Mayr, G.J., Fix, A. and Giez, A. (2008) On the onset of bora and the formation of rotors and jumps near a mountain gap. *Quarterly Journal of the Royal Meteorological Society*, 134, 21–46. https://doi.org/10.1002/qj.206.

Grell, G.A. and Freitas, S.R. (2013) A scale and aerosol aware stochastic convective parameterization for weather and air quality modeling. *Atmospheric Chemistry & Physics Discussions*, 13, 23845–23893. https://doi.org/10.5194/acp-14-5233-2014.

Hills, M.O. and Durran, D.R. (2012) Non-stationary trapped lee waves generated by the passage of an isolated jet. *Journal of the Atmospheric Sciences*, 69, 3040–3059. https://doi.org/10.1175/JAS-D-12-047.1.

Hines, K.M. and Bromwich, D.H. (2008) Development and testing of polar weather research and forecasting (WRF) model. Part I: Greenland ice sheet meteorology. *Monthly Weather Review*, 136, 1971–1989. https://doi.org/10.1175/2007MWR2112.1.

Hines, K.M., Bromwich, D.H., Bai, L., Bitz, C.M., Powers, J.G. and Manning, K.W. (2015) Sea ice enhancements to polar WRF. *Monthly Weather Review*, 143, 2363–2385. https://doi.org/10.1175/MWR-D-14-00344.1.

Hines, K.M., Bromwich, D.H., Bai, L.-S., Barlage, M. and Slater, A.G. (2011) Development and testing of polar WRF. Part III: Arctic land. *Journal of Climate*, 24, 26–48. https://doi.org/10.1175/2010JCLI3460.1.

Iacono, M.J., Delamere, J.S., Mlawer, E.J., Shephard, M.W., Clough, S.A. and Collins, W.D. (2008) Radiative forcing by long-lived greenhouse gases: calculations with the AER radiative transfer models. *Journal of Geophysical Research: Atmospheres*, 113(D13). https://doi.org/10.1029/2008JD009944.

IGRA. (2018) Integrated Global Radiosonde Archive, NOAA/NCEP. Available at: https://www.ncdc.noaa.gov/data-access/weather-balloon/integrated-global-radiosonde-archive; accessed 5 August 2019

Jiang, Q. (2014) Applicability of reduced-gravity shallow-water theory to atmospheric flow over topography. *Journal of the Atmospheric Sciences*, 71, 1460–1479. https://doi.org/10.1175/JAS-D-13-0101.1.

Kalnay, E., Kanamitsu, M., Kistler, R., Collins, W., Deaven, D., Gandin, L., Iredell, M., Saha, S., White, G., Woollen, J., Zhu, Y., Leetmaa, A., Reynolds, R., Chelliah, M., Ebisuzaki, W., Higgins, W., Janowiak, J., Mo, K.C., Ropelewski, C., Wang, J., Jenne, R. and Joseph, D. (1996) The NCEP/NCAR 40-year reanalysis project. *Bulletin of the American Meteorological Society*, 77, 437–472. https://doi.org/10.1175/1520-0477(1996)077<0437:TNYRP>2.0.CO;2.

Klemp, J., Dudhia, J. and Hassiotis, A. (2008) An upper gravity-wave absorbing layer for NWP applications. *Monthly Weather Review*, 136, 3987–4004. https://doi.org/10.1175/2008MWR2596.1.

Klemp, J. and Lilly, D. (1975) The dynamics of wave-induced downslope winds. *Journal of the Atmospheric Sciences*, 32, 320–339. https://doi.org/10.1175/1520-0469(1975)032<0320:TDOWID>2.0.CO;2.

Laprise, R. and Peltier, W. (1989) The linear stability of nonlinear mountain waves: implications for the understanding of severe downslope windstorms. *Journal of the Atmospheric Sciences*, 46, 545–564. https://doi.org/10.1175/1520-0469(1989)046<0545:TLSONM>2.0.CO;2.

Long, R.R. (1954) Some aspects of the flow of stratified fluids: II. Experiments with a two-fluid system. *Tellus A*, 6, 97–115. https://doi.org/10.1111/j.2153-3490.1954.tb01100.x.

Maslanik, J., Stroeve, J., Fowler, C. and Emery, W. (2011) Distribution and trends in Arctic Sea ice age through spring 2011. *Geophysical Research Letters*, 38(13). https://doi.org/10.1029/2011GL047735.

Mayr, G.J. and Gohm, A. (2000) 2D airflow over a double bell-shaped mountain. *Meteorology and Atmospheric Physics*, 72, 13–27. https://doi.org/10.1007/s007030050002.

Menchaca, M.Q. and Durran, D.R. (2017) Mountain waves, downslope winds, and low-level blocking forced by a midlatitude cyclone encountering an isolated ridge. *Journal of the Atmospheric Sciences*, 74, 617–639. https://doi.org/10.1175/JAS-D-16-0092.1.

Moore, G. (2016) The March 1972 northwest Greenland windstorm: evidence of downslope winds associated with a trapped lee wave. *Quarterly Journal of the Royal Meteorological Society*, 142, 1428–1438. https://doi.org/10.1002/qj.2744.

Morrison, H., Curry, J. and Khvorostyanov, V. (2005) A new double-moment microphysics parameterization for application in cloud and climate models. Part I: Description. *Journal of the Atmospheric Sciences*, 62, 1665–1677. https://doi.org/10.1175/JAS3446.1.

Mysak, L.A. and Manak, D.K. (1989) Arctic sea-ice extent and anomalies, 1953–1984. *Atmosphere-Ocean*, 27, 376–405. https://doi.org/10.1080/07055900.1989.9649342.

Nakanishi, M. and Niino, H. (2004) An improved Mellor–Yamada level-3 model with condensation physics: its design and verification. *Boundary-Layer Meteorology*, 112, 1–31. https://doi.org/10.1023/B:BOUN.0000020164.04146.98.

Niu, G.-Y., Yang, Z.-L., Mitchell, K.E., Chen, F., Ek, M.B., Barlage, M., Kumar, A., Manning, K., Niyogi, D., Rosero, E., Tewari, M. and Xia, Y. (2011) The community Noah land surface model with multiparameterization options (Noah-MP): 1. Model description and evaluation with local-scale measurements. *Journal of Geophysical Research: Atmospheres*, 116(D12). https://doi.org/10.1029/2010JD015140.

NunaGIS. (2018) Geographic information system for Greenland, Department of National Planning, Nuuk, Greenland. Available at: http://www.nunagis.gl/en/; accessed 5 August 2019

Peltier, W. and Clark, T. (1979) The evolution and stability of finite-amplitude mountain waves. Part II: Surface wave drag and severe downslope windstorms. *Journal of the Atmospheric Sciences*, 36, 1498–1529. https://doi.org/10.1175/1520-0469(1979)036<1498:TEASOF>2.0.CO;2.

Peltier, W. and Scinocca, J. (1990) The origin of severe downslope windstorm pulsations. *Journal of the Atmospheric Sciences*, 47, 2853–2870. https://doi.org/10.1175/1520-0469(1990)047<2853:TOOSDW>2.0.CO;2.

Reinecke, P.A. and Durran, D.R. (2009) Initial-condition sensitivities and the predictability of downslope winds. *Journal of the Atmospheric Sciences*, 66, 3401–3418. https://doi.org/10.1175/2009JAS3023.1.

Sachsperger, J., Serafin, S., Grubišić, V., Stiperski, I. and Paci, A. (2017) The amplitude of lee waves on the boundary-layer inversion. *Quarterly Journal of the Royal Meteorological Society*, 143, 27–36. https://doi.org/10.1002/qj.2915.

Schär, C. and Durran, D.R. (1997) Vortex formation and vortex shedding in continuously stratified flows past isolated topography. *Journal of the Atmospheric Sciences*, 54, 534–554. https://doi.org/10.1175/1520-0469(1997)054<0534:VFAVSI>2.0.CO;2.

Schär, C. and Smith, R.B. (1993) Shallow-water flow past isolated topography. Part I: Vorticity production and wake formation. *Journal of the Atmospheric Sciences*, 50, 1373–1400. https://doi.org/10.1175/1520-0469(1993)050<1373:SWFPIT>2.0.CO;2.

Scinocca, J. and Peltier, W. (1989) Pulsating downslope windstorms. *Journal of the Atmospheric Sciences*, 46, 2885–2914. https://doi.org/10.1175/1520-0469(1989)046<2885:PDW>2.0.CO;2.

Scorer, R.S. (1949) Theory of waves in the lee of mountains. *Quarterly Journal of the Royal Meteorological Society*, 75, 41–56. https://doi.org/10.1002/qj.49707532308.

Skamarock, W.C., Klemp, J.B., Dudhia, J., Gill, D.O., Barker, D.M., Duda, M.G., Huang, X.-Y., Wang, W. and Powers, J.G. (2008) A description of the Advanced Research WRF version 3, report TN-475+STR. NCAR, Boulder, CO. https://doi.org/10.5065/D68S4MVH.

Smith, R.B. (1985) On severe downslope winds. *Journal of the Atmospheric Sciences*, 42, 2597–2603. https://doi.org/10.1175/1520-0469(1985)042<2597:OSDW>2.0.CO;2.

Smith, R.B. (1991) Kelvin–Helmholtz instability in severe downslope wind flow. *Journal of the Atmospheric Sciences*, 48, 1319–1324. https://doi.org/10.1175/1520-0469(1991)048<1319:KHIISD>2.0.CO;2.

Stansfield, J.R. (1972) The severe Arctic storm of 8–9 March 1972 at Thule Air Force Base, Greenland. *Weatherwise*, 25, 228–232. https://doi.org/10.1080/00431672.1972.9931607.

Steinhoff, D.F., Bromwich, D.H. and Monaghan, A. (2013) Dynamics of the foehn mechanism in the McMurdo dry valleys of Antarctica from polar WRF. *Quarterly Journal of the Royal Meteorological Society*, 139, 1615–1631.

Stiperski, I., Serafin, S., Paci, A., Ágústsson, H., Belleudy, A., Calmer, R., Horvath, K., Knigge, C., Sachsperger, J., Strauss, L. and Grubišić, V. (2017) Water tank experiments on stratified flow over double mountain-shaped obstacles at high Reynolds number. *Atmosphere*, 8(1). https://doi.org/10.3390/atmos8010013.

Thorsteinsson, S. and Sigurdsson, S. (1996) Orogenic blocking and deflection of stratified air flow on an f-plane. *Tellus A*, 48, 572–583. https://doi.org/10.1034/j.1600-0870.1996.t01-3-00006.x.

Uppala, S.M., Kållberg, P.W., Simmons, A.J., Andrae, U., Bechtold, V.D., Fiorino, M., Gibson, J.K., Haseler, J., Hernandez, A., Kelly, G.A., Li X., Onogi K., Saarinen S., Sokka N., Allan R.P., Andersson

E., Arpe K., Balmaseda M.A., Beljaars A.C.M., Van de Berg L., Bidlot J., Bormann N., Caires S., Chevallier F., Dethof A., Dragosazac M., Fisher M., Fuentes M., Hagemann S., Hólm E.V., Hoskins B.J., Isaksen L., Janssen P.A.E.M., Jenne R., McNally A.P., Mahfouf J-F., Morcrette J-J., Rayner N.A., Saunders R.W., Simon P., Sterl A., Trenberth K.A., Untch A., Vasiljevic D., Viterbo P. and Woollen J. (2005) The ERA-40 re-analysis. *Quarterly Journal of the Royal Meteorological Society*, 131, 2961–3012. https://doi.org/10.1256/qj.04.176.

Vosper, S.B. (2004) Inversion effects on mountain lee waves. *Quarterly Journal of the Royal Meteorological Society*, 130, 1723–1748. https://doi.org/10.1256/qj.03.63.

Wagner, J., Gohm, A., Dörnbrack, A. and Schäfler, A. (2011) The mesoscale structure of a polar low: airborne lidar measurements and simulations. *Quarterly Journal of the Royal Meteorological Society*, 137, 1516–1531. https://doi.org/10.1002/qj.857.

Walsh, J.E. and Johnson, C.M. (1979) An analysis of Arctic Sea ice fluctuations, 1953–77. *Journal of Physical Oceanography*, 9, 580–591. https://doi.org/10.1175/1520-0485(1979)009<0580:AAOASI>2.0.CO;2.

Warren, S.G., Rigor, I.G., Untersteiner, N., Radionov, V.F., Bryazgin, N.N., Aleksandrov, Y.I. and Colony, R. (1999) Snow depth on Arctic Sea ice. *Journal of Climate*, 12, 1814–1829. https://doi.org/10.1175/1520-0442(1999)012<1814:SDOASI>2.0.CO;2.

Welch, P. (1967) The use of fast Fourier transform for the estimation of power spectra: a method based on time averaging over short, modified periodograms. *IEEE Transactions on Audio and Electroacoustics*, 15, 70–73. https://doi.org/10.1109/TAU.1967.1161901.

Zängl, G., Gohm, A. and Geier, G. (2004) South foehn in the Wipp Valley–Innsbruck region: numerical simulations of the 24 October 1999 case (MAP-IOP 10). *Meteorology and Atmospheric Physics*, 86, 213–243. https://doi.org/10.1007/s00703-003-0029-8.

Zhang, J. and Rothrock, D. (2003) Modeling global sea ice with a thickness and enthalpy distribution model in generalized curvilinear coordinates. *Monthly Weather Review*, 131, 845–861. https://doi.org/10.1175/1520-0493(2003)131<0845:MGSIWA>2.0.CO;2.

How to cite this article: Tollinger M, Gohm A, Jonassen MO. Unravelling the March 1972 northwest Greenland windstorm with high-resolution numerical simulations. *Q J R Meteorol Soc*. 2019;145:3409–3431. https://doi.org/10.1002/qj.3627